JCB Journal of Cell Biology

ARTICLE

# ENSA and ARPP19 differentially control cell cycle progression and development

Khaled Hached[1]*, Perrine Goguet[1]*, Sophie Charrasse[1], Suzanne Vigneron[1], Maria P. Sacristan[2], Thierry Lorca[1], and Anna Castro[1]

**Greatwall (GWL) is an essential kinase that indirectly controls PP2A-B55, the phosphatase counterbalancing cyclin B/CDK1 activity during mitosis. In *Xenopus laevis* egg extracts, GWL-mediated phosphorylation of overexpressed ARPP19 and ENSA turns them into potent PP2A-B55 inhibitors. It has been shown that the GWL/ENSA/PP2A-B55 axis contributes to the control of DNA replication, but little is known about the role of ARPP19 in cell division. By using conditional knockout mouse models, we investigated the specific roles of ARPP19 and ENSA in cell division. We found that *Arpp19*, but not *Ensa*, is essential for mouse embryogenesis. Moreover, *Arpp19* ablation dramatically decreased mouse embryonic fibroblast (MEF) viability by perturbing the temporal pattern of protein dephosphorylation during mitotic progression, possibly by a drop of PP2A-B55 activity inhibition. We show that these alterations are not prevented by ENSA, which is still expressed in *Arpp19*$^{\Delta/\Delta}$ MEFs, suggesting that ARPP19 is essential for mitotic division. Strikingly, we demonstrate that unlike ARPP19, ENSA is not required for early embryonic development. *Arpp19* knockout did not perturb the S phase, unlike *Ensa* gene ablation. We conclude that, during mouse embryogenesis, the *Arpp19* and *Ensa* paralog genes display specific functions by differentially controlling cell cycle progression.**

## Introduction

Mitotic entry and exit are controlled by the balance between the cyclin B/CDK1 kinase activity and its counteracting phosphatase PP2A-B55. At the G2/M transition, cyclin B/CDK1 activity increases, overriding PP2A-B55 activity to promote massive protein phosphorylation and mitotic entry (Ferrell, 2013; Mochida et al., 2016; Vigneron et al., 2018). Conversely, at anaphase onset, activation of anaphase-promoting complex/cyclosome (APC/C) induces cyclin B ubiquitination and degradation, resulting in the inactivation of cyclin B/CDK1 (Peters, 2006). Consequently, PP2A-B55 activity becomes predominant, leading to massive protein dephosphorylation and mitotic exit (Glover, 2012; Hunt, 2013; Lorca and Castro, 2013). First bibliographic data demonstrated that PP2A-B55 must be inhibited at mitotic entry (Mochida et al., 2009) and that this inhibition is promoted by the activation of Greatwall (GWL), although the mechanisms underlying this inhibition are unknown (Castilho et al., 2009; Vigneron et al., 2009; Burgess et al., 2010). Later results from two different laboratories first identified ARPP19 and ENSA as the substrates of GWL whose phosphorylation turns them into potent inhibitors of PP2A-B55 (Gharbi-Ayachi et al., 2010; Mochida et al., 2010). These authors first identified ARPP19 as a major GWL substrate, and then also ENSA, due to its high sequence homology with ARPP19. Although ARPP19 was the first identified GWL substrate, its putative involvement in the control of PP2A-B55 activity has been questioned because of its low endogenous expression and has been attributed to the most abundant protein ENSA (Mochida et al., 2010; Cundell et al., 2013). Nevertheless, depletion of ARPP19, but not of ENSA, from *Xenopus laevis* egg extracts prevents mitotic entry (Gharbi-Ayachi et al., 2010), and the GWL-ARPP19 axis seems to be required for meiotic maturation in porcine oocytes in which ENSA is not expressed (Li et al., 2013). However, in all these studies, ARPP19 was never specifically detected and was not discriminated from its paralog ENSA.

Beyond its role in mitotic progression, the GWL/ENSA/PP2A-B55 axis is also essential for S phase progression. Specifically, ENSA depletion from human cells promotes S phase extension associated with reduced replication fork density. This phenotype is induced by PP2A-B55–dependent dephosphorylation of one pivotal protein for the firing of replication origins: the replication factor treslin. Treslin dephosphorylation results in its degradation and in a decrease of the number of replicative forks (Charrasse et al., 2017). Conversely, it is not known whether ARPP19 also contributes to preventing treslin degradation during the S phase.

[1]Centre de Recherche de Biologie Cellulaire de Montpellier, Centre National de la Recherche Scientifique, Unité Mixte de Recherche 5237, Université de Montpellier, Montpellier, France; [2]Instituto de Biología Molecular y Celular del Cáncer, Universidad de Salamanca/Consejo Superior de Investigaciones Cientificas, Salamanca, Spain.

*K. Hached and P. Goguet contributed equally to this paper; Correspondence to Anna Castro: anna.castro@crbm.cnrs.fr; Thierry Lorca: thierry.lorca@crbm.cnrs.fr.

In this study, we determined ARPP19's role in mitotic division and DNA replication. We showed that *Arpp19* is essential for mouse development. Our data also indicate that in *Arpp19*$^{-/-}$ mouse embryonic fibroblasts (MEFs), mitotic entry is normal, but the substrate dephosphorylation kinetics during mitotic progression is altered. Strikingly, we demonstrate that unlike ARPP19, ENSA is not required for early embryonic development. Moreover, ARPP19 does not affect treslin stability, differently from ENSA. Altogether, these data suggest that during mouse embryogenesis, the *Arpp19* and *Ensa* paralogs would display specific functions by differentially controlling cell cycle progression.

## Results

### Arpp19 is present and functional in human cells

We produced an antibody against ARPP19 N terminus that does not cross-react with ENSA (Fig. S1 A). Endogenous ARPP19 was hardly detectable by Western blotting, but it was clearly visible when immunoprecipitated from HeLa cell extracts using this specific antibody (Fig. S1 A). To investigate ARPP19–PP2A-B55 binding, we immunoprecipitated ARPP19 using our antibody in a lysis buffer containing a reversible cross-linker to stabilize PP2A–ARPP19 complex and in which endogenous kinases are not active (with DTT and EDTA and without $Mg^{2+}$ or ATP). Endogenous ARPP19 bound to PP2A A, B55, and C, mainly during mitosis, particularly for the PP2A A subunit (Fig. 1 A). Then, to check the ARPP19 phosphorylation level at serine 62 (S62) induced by GWL, we immunoprecipitated ARPP19 using the previously described lysis buffer supplemented with microcystin to prevent ARPP19 dephosphorylation by PP2A-B55 (Williams et al., 2014). ARPP19 phosphorylated at S62 was hardly visible at the G1, S, and G2 phases but dramatically increased upon mitotic entry when GWL become fully active (Fig. 1 B). As expected, ARPP19 was gradually dephosphorylated during mitotic exit concomitantly with GWL inactivation (Fig. 1 C). Surprisingly, the addition of microcystin prevented ARPP19 dephosphorylation but also induced the dissociation of the PP2A A and C subunits from the PP2A–ARPP19 complex, despite the presence of the reversible cross-linker (Fig. 1 D). Because ARPP19 directly binds to B55 (Mochida, 2014), and PP2A A and C subunits are tightly associated (Xing et al., 2006), we hypothesized that cross-linking occurred mainly between the ARPP19/B55 and PP2A A/C subcomplexes and that microcystin binding to C subunit promoted the dissociation of these two subcomplexes. We took advantage of PP2A-B55 dissociation and inhibition by microcystin to precisely analyze the temporal pattern of ARPP19 dephosphorylation by adding microcystin to mitosis-synchronized cell lysates at different times after lysis. This strategy revealed that S62-ARPP19 dephosphorylation started as early as 5 min after lysis and was complete at 30 min (Fig. 1 D). Our results demonstrate that ARPP19 is expressed in human cells and that, upon phosphorylation on its GWL site, it binds to PP2A-B55.

### ARPP19, but not ENSA, is essential for embryonic development

Next, we generated a mouse model in which a "knockout-first" allele was inserted in the *Arpp19* gene (Skarnes et al., 2011). This *Arpp19* allele is predicted to generate a null allele through splicing to a *lacZ*-trapping element contained in the targeting allele and consequently to express β-galactosidase instead of ARPP19. We used this mouse model to determine *Arpp19* expression pattern during embryogenesis. We then generated a conditional knockout mouse for the *Arpp19* gene devoid of the selection cassette and with LoxP recombination sequences on both sites of the critical exon 4 of the *Arpp19* locus (hereafter referred to as *Arpp19*$^{Lox/Lox}$). This mouse was obtained by crossing *Arpp19* knockout-first mice with mice that ubiquitously express the Flp recombinase (Fig. 2, A and B). The ubiquitous deletion of *Arpp19* (hereafter referred as *Arpp19*$^{\Delta/\Delta}$) was obtained by mating *Arpp19*$^{Lox/Lox}$ mice with mice that constitutively express the Cre recombinase (Rosa26-Cre-GFP) or express a tamoxifen-inducible Cre recombinase (RNApolII-Cre ERT2; Guerra et al., 2003; Birling et al., 2012). We used this second mouse model to investigate ARPP19's role in vivo. *Arpp19*$^{Lox/\Delta}$ heterozygous mice were viable and fertile. Conversely, homozygous *Arpp19*$^{\Delta/\Delta}$ mice were never born when *Arpp19*$^{Lox/\Delta}$ heterozygous mice were intercrossed, suggesting that *Arpp19* deletion is embryonic lethal (Fig. 2 C). Analysis of 39 embryonic day 8.5 (E8.5) embryos from four different *Arpp19*$^{Lox/\Delta}$ heterozygous mice intercrosses (Fig. 2 D) showed that all *Arpp19*$^{Lox/Lox}$ embryos developed normally as well as most of the *Arpp19*$^{Lox/\Delta}$ heterozygote animals. Conversely, 100% of *Arpp19*$^{\Delta/\Delta}$ embryos presented severe abnormalities (Fig. 2 D, E8.5). Histological analysis at stages E8.5 and E10.5 revealed that in most *Arpp19*$^{\Delta/\Delta}$ embryos, gastrulation did not take place (Fig. 2 D, i, E8.5), and in the others, development arrested before embryo turning (Fig. 2, D, ii, E8.5 and E10.5). To determine whether mitosis was affected in these embryos, we crossed *Arpp19*$^{Lox/Lox}$ males with *Arpp19*$^{Wt/Lox}$ females both harboring the inducible RNApolII-Cre (ERT2). We then injected tamoxifen i.p. in pregnant females at E13 and recovered embryos at E17.5. Immunohistochemical analysis with an anti-phosphorylated histone H3 antibody showed that the number of mitotic cells in the epidermal basal layer was significantly increased in *Arpp19*$^{\Delta/\Delta}$ embryos compared with *Arpp19*$^{Lox/\Delta}$ littermates (Fig. 2 E), suggesting that mitosis progression was perturbed. We then investigated whether ARPP19 is required for development beyond gastrulation. For this, we crossed *Arpp19*$^{Lox/Lox}$ males with *Arpp19*$^{Wt/Lox}$ females harboring ERT2 (Guerra et al., 2003) and then injected tamoxifen in pregnant females at E7.5 and recovered embryos at E18.5. At this stage, the *Arpp19*$^{Wt/\Delta}$ embryos were normal, whereas the *Arpp19*$^{\Delta/\Delta}$ embryos were arrested at around E9 of development (Fig. 2 F), suggesting that *Arpp19* is necessary throughout development.

To test the possibility that ENSA also could be required for embryonic development, we generated a second mouse model in which a knockout-first allele was inserted in the *Ensa* gene (Fig. 2 G; Skarnes et al., 2011). ENSA knockout-first heterozygous mice were viable and fertile. Moreover, in *Ensa*-knockout embryos, development progressed normally at least until E8.5 and *Ensa*-knockout animals were born, although at a lower frequency than expected (Fig. 2, H and I).

These results suggest that only *Arpp19* is essential for early embryogenesis. Nevertheless, to investigate whether the absence of early defects in *Ensa*-knockout embryos could reflect the lack of expression of this protein during early development,

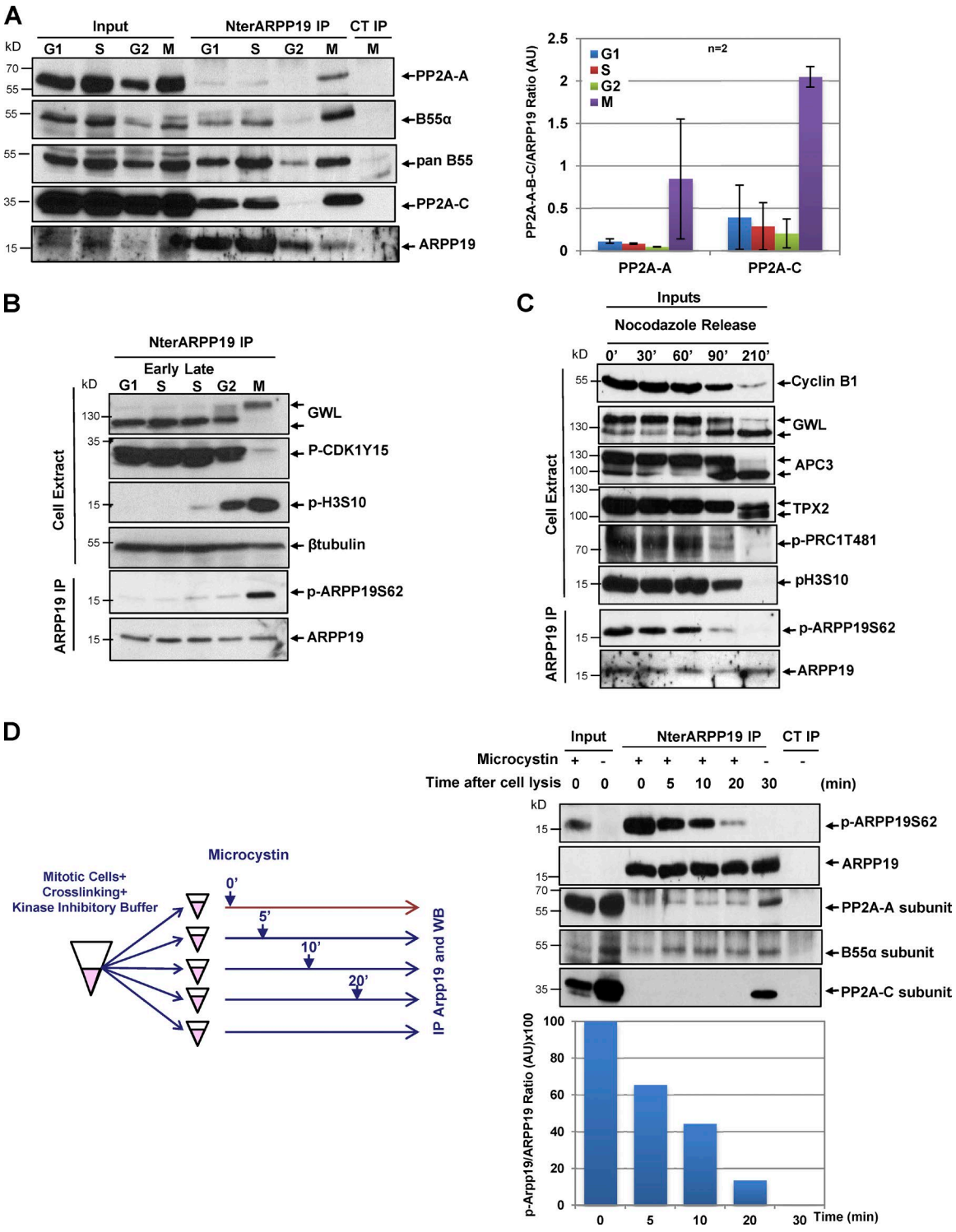


Figure 1. **ARPP19 is functional in human cells. (A)** Synchronized HeLa cells were lysed in the presence of a reversible cross-linker and used for immunoprecipitation (IP), using anti-NterARPP19 or anti-GST (control [CT]) antibodies. PP2A-B55 subunits and ARPP19 were checked in inputs and immunoprecipitates (IP). The levels of PP2A subunits A and C in the IPs were quantified using ImageJ software, normalized to the total levels of ARPP19, and represented. Values (mean ± SD) are from two different experiments. **(B)** HeLa cells were synchronized in G1 (24-h thymidine block), early S phase (2.5-h thymidine release), late S phase (6-h thymidine release), G2 (12-h RO3306 block), or M phase (12-h nocodazole shake-off) and lysed in the presence of a reversible cross-linker and microcystin. ARPP19 IPs and whole-cell extracts were used for Western blotting. **(C)** Nocodazole-blocked HeLa cells were released, lysed in the presence of microcystin, and used for IP. Inputs and IP were analyzed by Western blotting with the indicated antibodies. **(D)** Mitotic-enriched cell populations were lysed in the presence of a reversible cross-linker, and then microcystin was added (or not) at different time points, as indicated in the scheme, before IP using anti-NterARPP19 or anti-GST (CT) antibodies. Inputs and IPs were then used for Western blotting. The phosphorylated ARPP19 at S62/total ARPP19 ratio intensities at different time points after cell lysis of this experiment are shown in the lower graph. Data are representative of two different experiments.

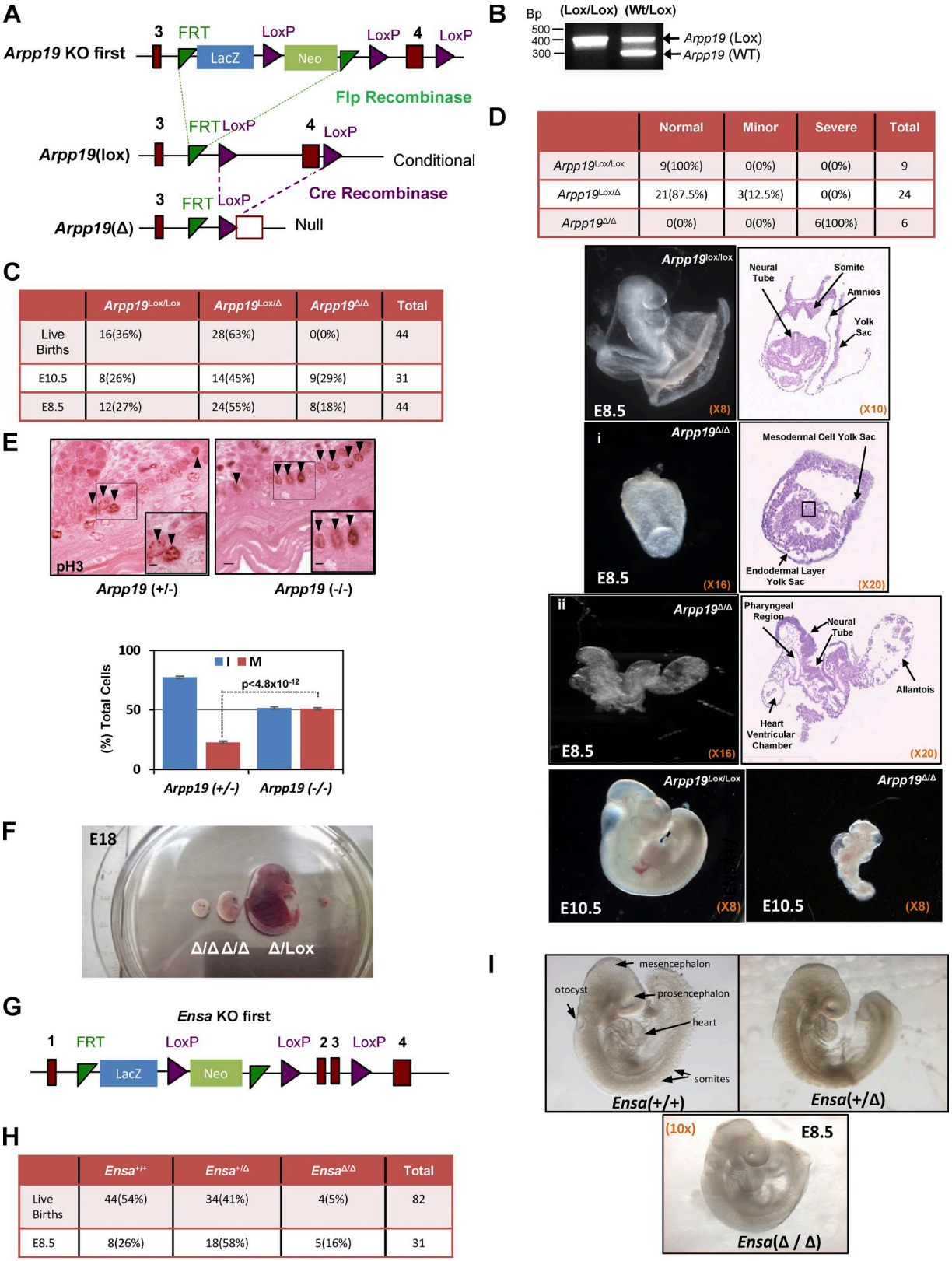


| | Arpp19$^{Lox/Lox}$ | Arpp19$^{Lox/Δ}$ | Arpp19$^{Δ/Δ}$ | Total |
|---|---|---|---|---|
| Live Births | 16(36%) | 28(63%) | 0(0%) | 44 |
| E10.5 | 8(26%) | 14(45%) | 9(29%) | 31 |
| E8.5 | 12(27%) | 24(55%) | 8(18%) | 44 |

| | Normal | Minor | Severe | Total |
|---|---|---|---|---|
| Arpp19$^{Lox/Lox}$ | 9(100%) | 0(0%) | 0(0%) | 9 |
| Arpp19$^{Lox/Δ}$ | 21(87.5%) | 3(12.5%) | 0(0%) | 24 |
| Arpp19$^{Δ/Δ}$ | 0(0%) | 0(0%) | 6(100%) | 6 |

| | Ensa$^{+/+}$ | Ensa$^{+/Δ}$ | Ensa$^{Δ/Δ}$ | Total |
|---|---|---|---|---|
| Live Births | 44(54%) | 34(41%) | 4(5%) | 82 |
| E8.5 | 8(26%) | 18(58%) | 5(16%) | 31 |

Figure 2. **ARPP19, but not ENSA, is essential for embryogenesis. (A)** The knockout first (KO-first) allele (Tm1a allele) was converted into a conditional allele that does not harbor the selection cassette by mating heterozygous Arpp19$^{tm1a(KOMP)Mbp}$ mice with Gt(ROSA)26Sor$^{tm1(FLP1)Dym/Wtsi}$ mice. Exon 4 of the murine *Arpp19* gene was then flanked by LoxP sequences (violet triangles), and Cre-mediated recombination resulted in *Arpp19*-null alleles. **(B)** Representative PCR products of WT *Arpp19* and floxed alleles (Lox). **(C)** Number (percentage) of live births and embryos recovered at the indicated developmental stages from heterozygous crosses between *Arpp19*$^{Wt/Δ}$ mice. **(D)** Statistics of the different phenotypes observed for the indicated mouse genotypes. Representative images of E8.5 and E10.5 *Arpp19*$^{Lox/Lox}$ and *Arpp19*$^{Δ/Δ}$ embryos from heterozygous crosses confirmed by genotyping. Histological sections from the indicated embryos

we took advantage of *Arpp19* and *Ensa*–knockout-first mice in which β-galactosidase is expressed from these alleles under the control of the endogenous promoters. Whole-mount β-galactosidase staining of E6.5 embryos showed an equivalent activity of both *Arpp19* and *Ensa* promoters in the embryonic and to a lesser extent in the extraembryonic tissues (Fig. S1 B), suggesting that *Ensa* and *Arpp19* would be similarly expressed in these embryos.

### *Arpp19* is essential for MEF viability

To investigate ARPP19's role in cell cycle control during embryogenesis, we purified and immortalized *Arpp19*$^{Lox/Lox}$ MEFs. Immortal *Arpp19*$^{Lox/Lox}$ MEFs displayed normal cell proliferation and viability. By using recombinant His-ARPP19 as a calibration standard and immunoprecipitation with the NterArpp19 antibody, we estimated that in MEFs, endogenous ARPP19 amount was 0.06 ng/µg total protein (Fig. S1 C), a concentration close to the one reported by Cundell et al. (2013) in HeLa cells (<0.03 ng/µg). Infection of *Arpp19*$^{Lox/Lox}$ MEFs with a GFP-Cre–expressing adenovirus induced ARPP19 depletion in 72 h (Fig. 3 A) and significantly reduced cell viability (Fig. 3 B). Viability was restored when ARPP19, but not ARPP19-S62A (a nonphosphorylatable ARPP19 mutant in the GWL phosphorylation site), was ectopically reexpressed in *Arpp19*$^{Δ/Δ}$ MEFs. Thus, ARPP19 depletion specifically affects viability, and this phenotype depends on its phosphorylation by the GWL kinase.

### ARRP19 does not participate in the control of S phase progression

We next checked whether ARPP19 participated in S phase progression during embryogenesis. As previously described, we observed a dramatic decrease of treslin levels in U20S and HeLa cells upon *Ensa* silencing (Fig. 3 C). Treslin expression was also strongly reduced in *Gwl* and *Ensa*-knockout MEFs (Fig. 3 D), but not in *Arpp19*$^{Δ/Δ}$ MEFs, suggesting that ARPP19 may not be involved in the control of the S phase. Accordingly, *Arpp19*$^{Lox/Lox}$ and *Arpp19*$^{Δ/Δ}$ MEFs displayed similar FACS profiles and temporal patterns of EdU incorporation (Fig. 3, E and F). Moreover, ENSA nuclear staining significantly increased during the S phase and clearly colocalized with EdU staining in HeLa cells. Conversely, ARPP19 nuclear staining was not modified during DNA replication and did not colocalize with replication forks (Fig. 3 G). Together, these results suggest that ARPP19 is not involved in the control of S phase progression in MEFs and probably also in adult somatic cells and highlight the possibility that these two paralogs could display different regulations or physiological functions.

### ARPP19 is crucial for mitotic division in MEFs

To investigate whether ARPP19 plays an important role in mitosis, we monitored by time-lapse microscopy the mitotic division of *Arpp19*-knockout MEFs. We did not observe any difference in the mitotic entry kinetics between *Arpp19*$^{Δ/Δ}$ and control MEFs (Fig. 4 A), again supporting passage through the S phase with normal kinetics. Conversely, mitosis was significantly extended in the *Arpp19*$^{Δ/Δ}$ cells (Fig. 4 B). *Arpp19*$^{Δ/Δ}$ MEFs entered mitosis normally, but then showed important defects during mitotic progression, particularly loss of chromosome condensation. Specifically, chromosome condensation appeared to be normal at mitotic entry, but it was lost during prometaphase (Fig. 4 C, Misalignment and condensation defects; and Videos 1 and 2) or later during anaphase (Fig. 4 C, Massive segregation and condensation defects; and Video 3), leading to missegregation of decondensed DNA, which we refer to hereinafter as "massive defects." We also observed DNA bridges, chromosome misalignment, and segregation defects in *Arpp19*$^{Δ/Δ}$ MEFs with correctly condensed DNA (Fig. 4 C, DNA bridges and Misalignment and missegregation; and Videos 4 and 5), as well as a significant number of multinucleated *Arpp19*$^{Δ/Δ}$ MEFs and the presence of micronuclei (Fig. 4 D). These defects did not result from deficient spindle assembly checkpoint activity, because *Arpp19*-depleted MEFs were normally blocked at prometaphase by nocodazole treatment and showed normal cyclin B levels and cyclin B/CDK1 activity (Fig. 5 A, cyclin B; and see Fig. 7 D). Moreover, we noted that BUBR1 signal intensity at kinetochores was not decreased but rather increased in *Arpp19*$^{Δ/Δ}$ MEFs, confirming the presence of an active spindle assembly checkpoint in these cells (Fig. 4 E). We observed a similar massive defect phenotype in primary *Arpp19*$^{Δ/Δ}$ MEFs (Fig. S2 A), supporting the robustness of our experimental models.

Quantification of these phenotypes showed that 53% of *Arpp19*$^{Δ/Δ}$ (GFP-Cre) MEFs exhibited abnormal mitoses compared with 18% of the control cells (Fig. 4 F). Chromosome misalignments were 3.5 times more frequent, and missegregation and DNA bridges 50% higher, in *Arpp19*$^{Δ/Δ}$ cells compared with controls (GFP). Moreover, massive defects were present in 13% of *Arpp19*$^{Δ/Δ}$ MEFs and only 6% of control cells (Fig. 4 F), and micronuclei and binucleated cells in 28% and 13% of *Arpp19*$^{Δ/Δ}$ cells compared with 3% of controls (Fig. 4 D). Finally, we detected chromosome decondensation in only 0.6% of control cells versus 16% in *Arpp19*$^{Δ/Δ}$ MEFs (Fig. 4, F and G). DNA decondensation was mostly associated with massive defects, whereas misalignment, missegregation, and/or DNA bridges were associated with normally condensed chromosomes (Fig. 4 H).

We next investigated the effect of ARPP19 loss on PP2A-B55 activity by measuring CDK substrate phosphorylation (phospho-

were stained with hematoxylin-eosin, and images were acquired with a transmitted light microscope. Magnifications are indicated in the images. **(E)** Immunohistochemical analysis of mitotic (M), phosphorylated histone H3 signal (pH3), and interphasic (I) cells in the epidermal basal layer of E17.5 *Arpp19*$^{Wt/Δ}$ and *Arpp19*$^{Δ/Δ}$ embryos. Data are the mean ± SD of two different experiments (five embryos for each genotype/experiment). Bar, 10 µm. Bar magnifications, 5 µm. **(F)** Representative images of E18 *Arpp19*$^{Δ/Lox}$ and *Arpp19*$^{Δ/Δ}$embryos in which *Arpp19* was deleted in embryos by tamoxifen injection of pregnant *Arpp19*$^{Lox/Wt}$ PolII Cre ERT2 females at E7.5 after mating with *Arpp19*$^{Lox/Lox}$ RNApolII Cre ERT2$^{Ki/Ki}$ males (three experiments). **(G)** Schematic representation of the *Ensa* KO-first allele (Tm1a) that encodes LacZ instead of the ENSA protein under the control of its endogenous promoter. **(H)** Distribution of genotyped embryos obtained from crossing two heterozygous *Ensa* KO-first mice (results from three independent intercrosses). Of note, although all embryos were normal at E8.5, the genotype distribution does not follow the Mendelian ratio owing to failure of genotyping three embryos. **(I)** Representative light microscopy images of *Ensa* WT, heterozygous, and knockout E8.5 embryos obtained from mating *Ensa* heterozygous Tm1a mice. Magnification is indicated in the figure.

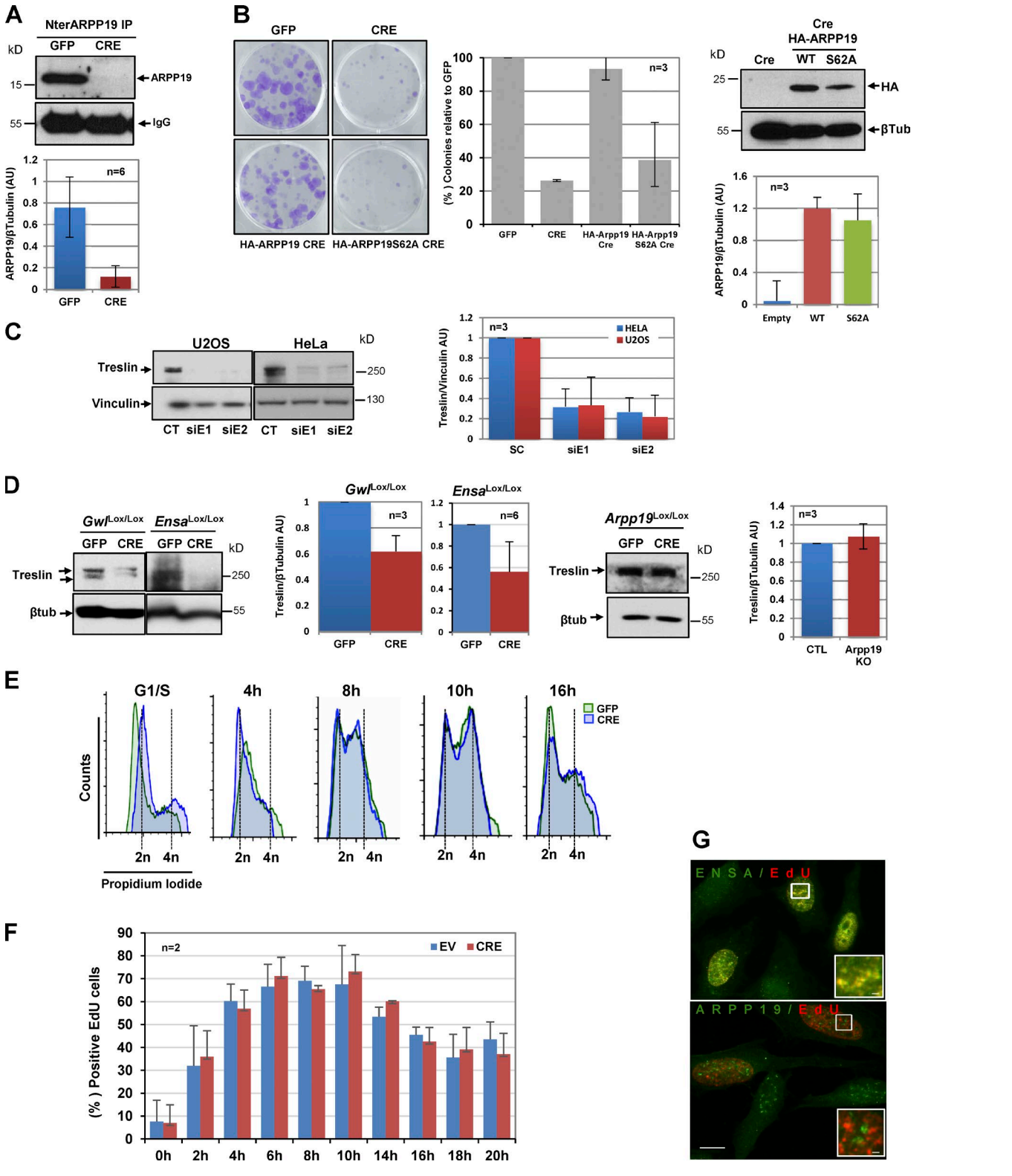


Figure 3. ***Arpp19* deletion decreases MEF viability without affecting S phase progression. (A)** *Arpp19*$^{Lox/Lox}$ MEFs were transduced with GFP- (GFP) or GFP-Cre–expressing (CRE) adenoviruses, and GFP-positive cells were sorted by FACS. ARPP19 expression was evaluated by immunoprecipitation (IP) using the anti-NterARPP19 antibody at day 3 after viral transduction. Band intensity was quantified from six independent experiments. **(B)** Clonogenic assays using critical dilutions of GFP or Cre MEFs. *Arpp19*$^{\Delta/\Delta}$ MEFs were transiently transfected with HA-ARPP19 or the HA-ARPP19 S62A mutant. Cell colonies were counted and plotted as percentages relative to GFP cells. Values are from three different experiments. Expression of HA-ARPP19 and HA-ARPP19 S62A was confirmed by Western blotting. Band intensities measured from three different experiments. **(C)** HeLa and U2OS cells were transfected with scramble (CT) or with two different siRNAs against *ENSA* (siE1 and siE2) and processed for Western blotting. **(D)** *Gwl*, *Ensa*, or *Arpp19* floxed MEFs were transduced with the indicated adenoviruses and used for treslin analysis by Western blotting ($n$ = 3, 6, and 3, respectively). **(E)** *Arpp19* floxed MEFs were transduced with GFP-Cre

S-CDK) by Western blotting and immunofluorescence. In *Arpp19*$^{\Delta/\Delta}$ MEFs (Cre) phosphorylation of CDK substrates was significantly decreased compared with control cells (Fig. 5 A; GFP), although cyclin B levels and cyclin B/CDK1 activity were not affected (Fig. 5 B). Nevertheless, residual CDK1-dependent phosphorylation was still present. Besides ARPP19, ENSA is phosphorylated by GWL and contributes to PP2A-B55 inhibition and mitotic progression (Gharbi-Ayachi et al., 2010; Mochida et al., 2010). We thus checked whether the CDK-dependent residual phosphorylation observed in *Arpp19*$^{\Delta/\Delta}$ cells could be due to ENSA phosphorylation. ENSA protein levels were comparable in *Arpp19*$^{\Delta/\Delta}$ and control MEFs (Fig. 5 C). On the other hand, ARPP19/ENSA phosphorylation on the GWL site was significantly decreased in *Arpp19*$^{\Delta/\Delta}$ cells. The residual phosphorylation signal suggests that ENSA could be partially phosphorylated in *Arpp19*$^{\Delta/\Delta}$ MEFs and could partly inhibit PP2A-B55 activity. However, this inhibition might not be sufficient for normal mitotic progression, because these cells displayed dramatic mitotic defects.

We next tested whether ARPP19/ENSA phosphorylation and the mitotic phenotypes could be rescued by overexpressing WT ARPP19 or the ARPP19-S62A mutant. ARPP19/ENSA phosphorylation in *Arpp19*$^{\Delta/\Delta}$ cells increased only upon overexpression of WT ARPP19 (Fig. 5 D). Moreover, the percentage of cells with normal mitotic progression significantly increased in *Arpp19*$^{\Delta/\Delta}$ MEFs after expression of WT ARPP19, but not of the ARPP19-S62A mutant (Fig. 5 E). This result demonstrates that ARPP19, via its phosphorylation by GWL, is essential for promoting normal mitosis progression in MEFs. Finally, to determine whether the mitotic cell defects induced by *Arpp19* ablation were the consequence of PP2A-B55 continuous/deregulated activity, we incubated cells with low doses of the PP2A-B55 inhibitor okadaic acid (OA). The addition of this inhibitor restored the percentage of cells with normal mitosis in *Arpp19*$^{\Delta/\Delta}$ MEFs (Fig. 5 F), suggesting that the observed mitotic phenotypes are the result of PP2A-B55 deregulated activity.

### Partially decondensed DNA in *Arpp19*$^{\Delta/\Delta}$ MEFs is associated with dephosphorylation of histone H3 and of the condensin II subunit CAPD3

To investigate the partial DNA decondensation in *Arpp19*$^{\Delta/\Delta}$ MEFs in more detail, we obtained chromosome spreads of *Arpp19*$^{\Delta/\Delta}$ MEFs (Fig. 6 A). We observed long chromosomes that were partially decondensed in *Arpp19*$^{\Delta/\Delta}$ MEFs. In some cases, such chromosomes acquired a spaghetti-like shape that we qualified as "major condensation defects." To determine the underlying mechanisms, we first checked the phosphorylation level of histone H3 on S10 (H3S10; Wei et al., 1999; Mellone et al., 2003). Western blot and immunofluorescence analyses showed that H3S10 phosphorylation was partially reduced in *Arpp19*$^{\Delta/\Delta}$ MEFs compared with control (Fig. S2 B). Incubation with low doses of the PP2A inhibitor OA restored H3S10 phosphorylation, suggesting that its dephosphorylation could be a direct or indirect consequence of PP2A deregulated activity.

The localization of the condensin complex at chromatin and the phosphorylation of its subunit CAPD3 are also required for correct DNA condensation (Kschonsak and Haering, 2015). At mitotic entry, CAPD3 phosphorylation on T1415 by cyclin B/CDK1 primes its further phosphorylation by PLK1 to increase CAPD3 supercoiling activity (St-Pierre et al., 2009; Abe et al., 2011). Moreover, CAPD3 is dephosphorylated by PP2A-B55 (Yeong et al., 2003). Analysis of CAPD3 localization, and phosphorylation showed that at prometaphase, CAPD3 was localized at chromosomes in both *Arpp19*$^{\Delta/\Delta}$ and control MEFs (Fig. 6 B). However, CAPD3 phosphorylation at T1415 (the cyclin B/CDK1 site) was strongly decreased in *Arpp19*$^{\Delta/\Delta}$ cells (Fig. 6 C). The activating phosphorylation of PLK1 on T210 also was reduced in *Arpp19*$^{\Delta/\Delta}$ cells, and its level was restored by incubation with the PP2A inhibitor OA (Fig. 6 D). These data suggest that PP2A-B55 deregulated activity upon *Arpp19* ablation contributes to the partial chromatin decondensation by preventing CAPD3 phosphorylation on T1415. In addition, as PLK1-dependent phosphorylation of CAPD3 controls its supercoiling activity, decreased PLK1 phosphorylation in *Arpp19*$^{\Delta/\Delta}$ MEFs could affect not only mitotic entry and progression, but also DNA condensation.

### *Arpp19* ablation promotes premature dephosphorylation of key cyclin B/CDK1 substrates and disrupts the temporal order of events during mitotic exit

Besides DNA decondensation, *Arpp19*$^{\Delta/\Delta}$ MEFs showed cytokinesis defects (DNA bridges or missegregated chromosomes), leading to multinucleated cells or the formation of micronuclei. These phenotypes could be partially explained by the chromatin condensation defect; however, as PP2A-B55 is essential for the dephosphorylation of cyclin B/CDK1 substrates (Mochida et al., 2009; Burgess et al., 2010; Cundell et al., 2013), we investigated whether the premature dephosphorylation of key proteins involved in mitotic exit could contribute to these disorders. Analysis of the kinetics of cyclin B/CDK1 substrate dephosphorylation at mitotic exit showed that in nocodazole-arrested *Arpp19*$^{\Delta/\Delta}$ MEFs, basal cyclin B/CDK1 substrate phosphorylation was decreased, and their dephosphorylation was advanced by 30 min after nocodazole release compared with controls (Fig. 7 A). In addition, APC3, a key APC/C component, the phosphorylation of which is required for APC/C activity, was quickly dephosphorylated in *Arpp19*$^{\Delta/\Delta}$ cells compared with control. This dephosphorylation was associated with complete degradation of securin and cyclin A (already at prometaphase). However, cyclin B was only partially degraded, and residual cyclin B/CDK1 complex was still left, as judged by the partial

or GFP-expressing adenoviruses, kept in G0 for 72 h, and then forced to reenter the cell cycle and blocked at the S-phase boundary by aphidicolin. After aphidicolin washout, MEFs were harvested and processed for FACS analysis. **(F)** MEFs in E were pulsed with EdU for 30 min and, at the indicated time points after aphidicolin release, were analyzed by immunostaining using anti-EdU antibodies and ImageJ software for quantification of the percentage of EdU-positive cells over time. **(G)** EdU-pulsed HeLa cells were fixed and counterstained with anti-ENSA or anti-ARPP19 (green) and anti-EdU (red) antibodies (1–2 mm confocal sections). Insets represent zooms of the boxed areas using ImageJ. Bar, 10 µm. Bar magnifications, 1 µm. All band intensities were quantified by densitometry using ImageJ and normalized to loading control. All data are means ± SD from the indicated number of experiments (n).

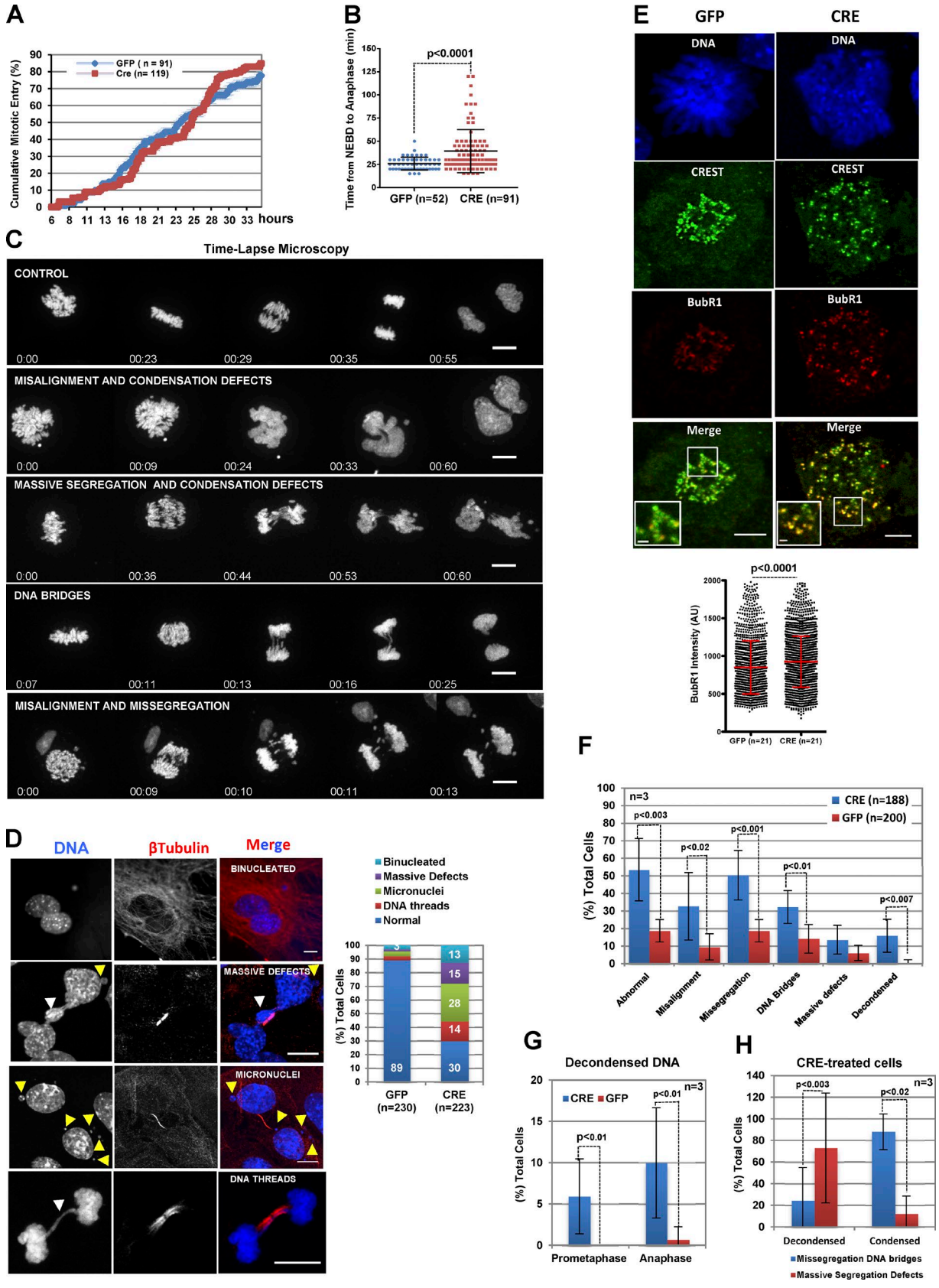


Figure 4. ***Arpp19* ablation induces dramatic mitotic phenotypes. (A)** *Arpp19*$^{Lox/Lox}$ MEFs that express H2B-mCherry were transduced with GFP or GFP-Cre adenoviruses and kept in starvation conditions. After 3 d, cells were forced to reenter the cell cycle. Cell morphology and chromosomes were monitored by live microscopy every 5 min using transmitted light and 561-nm LED, respectively. The percentage of cells entering mitosis (based on cell rounding and chromosome condensation) over time was quantified by analyzing time-lapse images. **(B)** Mitosis duration (in minutes; mean ± SEM of four biological replicates) was

rephosphorylation of CDK1 on tyrosine 15 in *Arpp19*$^{\Delta/\Delta}$ MEFs (Fig. 7 A). Finally, PRC1, a substrate of cyclin B/CDK1 and PP2A-B55 essential for cytokinesis (Jiang et al., 1998; Cundell et al., 2013), was not phosphorylated in prometaphase-arrested *Arpp19*$^{\Delta/\Delta}$ cells. PRC1 dephosphorylation was associated with mislocalization of this protein and also of its partner Aurora B kinase, during cytokinesis (Fig. 7, B and C). Specifically, during anaphase, Aurora B and PRC1 were localized in a broader central spindle zone in *Arpp19*$^{\Delta/\Delta}$ cells compared with control cells (Fig. 7, B and C). Moreover, in *Arpp19*$^{\Delta/\Delta}$ MEFs, we observed multiple or mislocalized Aurora B– or PRC1-positive structures that could correspond to cytokinesis furrows (Fig. 7, B and C, arrows), a phenotype never observed in controls.

Dephosphorylation of APC3 and PRC1 was not caused by faster inactivation of cyclin B/CDK1, based on in vitro analysis of the activity of this complex in *Arpp19*$^{\Delta/\Delta}$ MEFs (Fig. 7 D) and on cyclin B/CDK1-dependent PP1 phosphorylation at Thr320 (an autodephosphorylation PP1 site; Wu et al., 2009; Fig. 7 A). Incubation of *Arpp19*$^{\Delta/\Delta}$ MEFs with OA restored substrate phosphorylation by CDK1 as well as PRC1 and APC3 phosphorylation in prometaphase (Fig. 7 E), suggesting that dephosphorylation of these substrates may be the result of PP2A-B55 deregulated activity due to *Arpp19* depletion.

### *Arpp19* deletion perturbs the phosphorylation and localization of key nuclear envelope proteins

The phosphorylation state of key CDK substrates, such as lamins and nucleoporins (NUPs), dictates the temporal reformation of the nuclear envelope. The temporal localization of these proteins to chromosomes at late mitosis is dependent on their dephosphorylation (Heald and McKeon, 1990). CDK1-dependent phosphorylation of lamins A/C and NUPs was significantly reduced in *Arpp19*$^{\Delta/\Delta}$ MEFs compared with control cells (Fig. 8, A and B). This was associated with earlier NUP localization to the chromosomes during anaphase A, as opposed to anaphase B in control cells (Fig. 8 C). Moreover, during anaphase B, lamin A/C localization to DNA was slightly increased in *Arpp19*$^{\Delta/\Delta}$ MEFs compared with control cells (although not significantly). In *Arpp19*$^{\Delta/\Delta}$ MEFs, the earlier NUP localization to chromosomes resulted in the formation of a nuclear envelope that assembled nuclei or micronuclei. These results suggest that nuclear envelope reassembly in *Arpp19*$^{\Delta/\Delta}$ MEFs is advanced owing to the earlier NUP dephosphorylation and could contribute to the mitotic defects observed in these cells. Together, these data suggest that *Arpp19* ablation induces the earlier activation of PP2A-B55 that prematurely dephosphorylates key mitotic substrates, resulting in the disruption of the temporal order of the cellular events required for correct mitotic progression.

## Discussion

The first role attributed to the GWL kinase was the inhibition of the phosphatase PP2A-B55 during mitosis, although the underlying mechanism was initially unknown. The elucidation of GWL's mechanism of action significantly progressed by the identification of its substrates. Two laboratories (Gharbi-Ayachi et al., 2010; Mochida et al., 2010) identified ARPP19 as the first GWL substrate, and then ENSA by sequence homology analysis. Both studies demonstrated that phosphorylation of ectopic ARPP19 and ENSA promotes their binding to PP2A-B55 and inhibition of this phosphatase. Although both ectopic ARPP19 and ENSA were phosphorylated to the same extent and bound equally to PP2A-B55, the putative physiological role of the endogenous proteins in mitotic division was not clearly established. Indeed, only ARPP19 was identified by mass spectrometry. Moreover, ENSA depletion did not have any effect on mitotic division according to one of the two laboratories (Gharbi-Ayachi et al., 2010), whereas it blocked entry into mitosis according to the other (Mochida et al., 2010).

Interestingly, the genes encoding ARPP19 and ENSA appear to derive from the duplication of an ancestral gene in bilateral animals (http://www.ensembl.org; http://www.treefam.org). These genes then evolved through new duplications or losses, thus providing a variable number of homologues in the different species. In some species, such as *Drosophila melanogaster*, only one gene is conserved and it encodes the protein Endos, whose unique role reported so far is the control of mitosis (Kim et al., 2012). Some other species, such as *Saccharomyces cerevisiae,* have two different endosulfine genes that encode the proteins Igo1 and Igo2. These proteins share a similar function in the control of mitotic entry (Juanes et al., 2013; Chica et al., 2016), but they also display additional roles in the activation of G0 entry and in G1/S transition upon nutrient deprivation (Talarek et al., 2010, 2017). This last function is shared by Igo1, the unique endosulfine present in *Schizosaccharomyces pombe* (Martín et al., 2017).

The specific function of ARPP19 and ENSA is not known in mammalian cells. Because of its low expression, it has been assumed that ARPP19 is dispensable and that only ENSA is required for mitotic progression (Cundell et al., 2013). However, the involvement of ARPP19 in PP2A-B55 inhibition and cell cycle

calculated as the time from cell rounding and onset of chromosome condensation to chromosome segregation. **(C)** Mitotic progression was monitored in cells treated as in A, using live spinning-disk confocal microscopy. Representative still images of the different phenotypes observed in Videos 1, 2, 3, 4, and 5. Time after prometaphase onset is indicated. **(D)** Representative confocal sections of *Arpp19*$^{Lox/Lox}$ MEFs transduced with GFP or GFP-Cre adenoviruses. Bars, 10 µm. Cells exhibiting the indicated phenotypes were counted and are represented in a bar graph. **(E)** Cells in D were used for immunocytochemistry with anti-CREST and anti-BUBR1 antibodies and DAPI staining. Images were acquired by confocal microscopy. Spots corresponding to BUBR1 expression were automatically detected with Imaris in 3D images and manually corrected using CREST staining. The mean BUBR1 signal intensities were exported to Excel files for further analysis. The histogram shows the quantification of BUBR1 signal intensities (mean ± SD from 1,359 and 1,750 kinetochores from two biological replicates). Bars, 5 µm. Bar magnifications, 1 µm. **(F)** The spinning disk confocal movies from three different experiments were analyzed to quantify the number of cells displaying normal mitosis or the indicated phenotypes and are represented as the percentage of total cells (GFP or GFP-Cre). **(G)** Cells in C that underwent decondensation in prometaphase or after anaphase onset were counted and are represented. **(H)** GFP-Cre–expressing cells showing normally condensed or decondensed chromosomes were classified according to the indicated mitotic phenotypes.

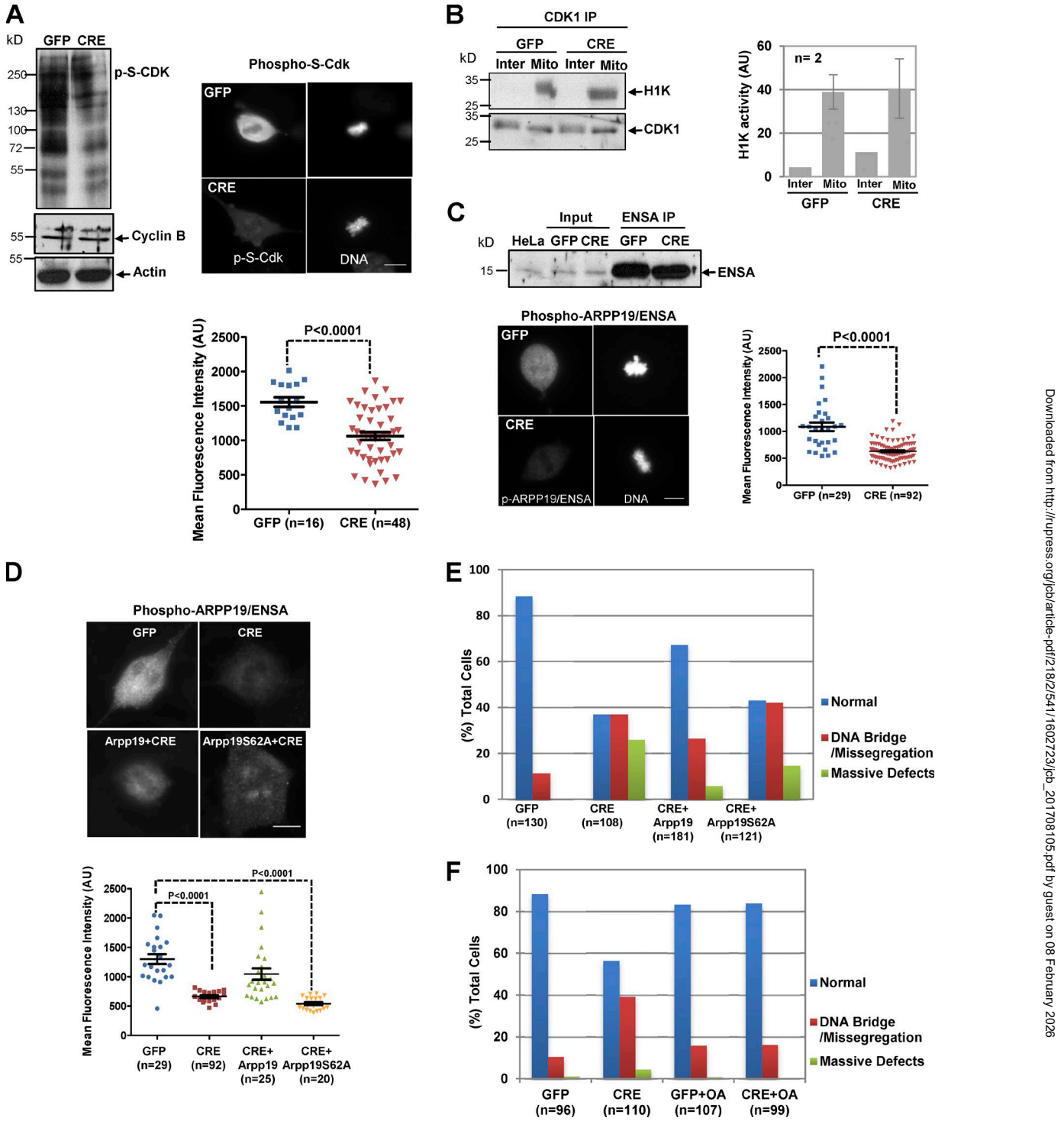


Figure 5. ***Arpp19* ablation phenotypes are rescued by inhibiting the PP2A phosphatase and by the ectopic expression of WT ARPP19, but not of the ARPP19S62A mutant. (A)** GFP and CRE mitotic *Arpp19*$^{Lox/Lox}$ MEFs obtained by nocodazole shake-off were lysed and analyzed by Western blotting (left) with the indicated antibodies (p-S-CDK, antibody to detect phosphorylation on serine residues by CDK) or by immunofluorescence (right), and the total p-S-CDK immunofluorescence signal was quantified. **(B)** CDK1 activity was assessed by IP in the indicated mitotic MEF lysates followed by histone H1 phosphorylation. Total cell signal was quantified. **(C)** Top: ENSA protein levels were measured in GFP and CRE MEF lysates and ENSA IPs by Western blotting. Bottom left panel: ARPP19/ENSA phosphorylation at the GWL site was measured by immunofluorescence. Bottom right: Total immunofluorescence signal was measured in control and *Arpp19*$^{\Delta/\Delta}$ MEFs using ImageJ and is represented as the means ± SEM. **(D)** As for C, except that *Arpp19*$^{\Delta/\Delta}$ cells ectopically express HA-tagged WT human ARPP19 or the S62A mutant. **(E)** Quantification of the phenotypes observed in MEFs from D. Data pooled from two different experiments. **(F)** GFP or CRE MEFs were incubated with 5 nM OA and used for immunofluorescence. Phenotypes were counted and are represented. Bars, 10 µm.

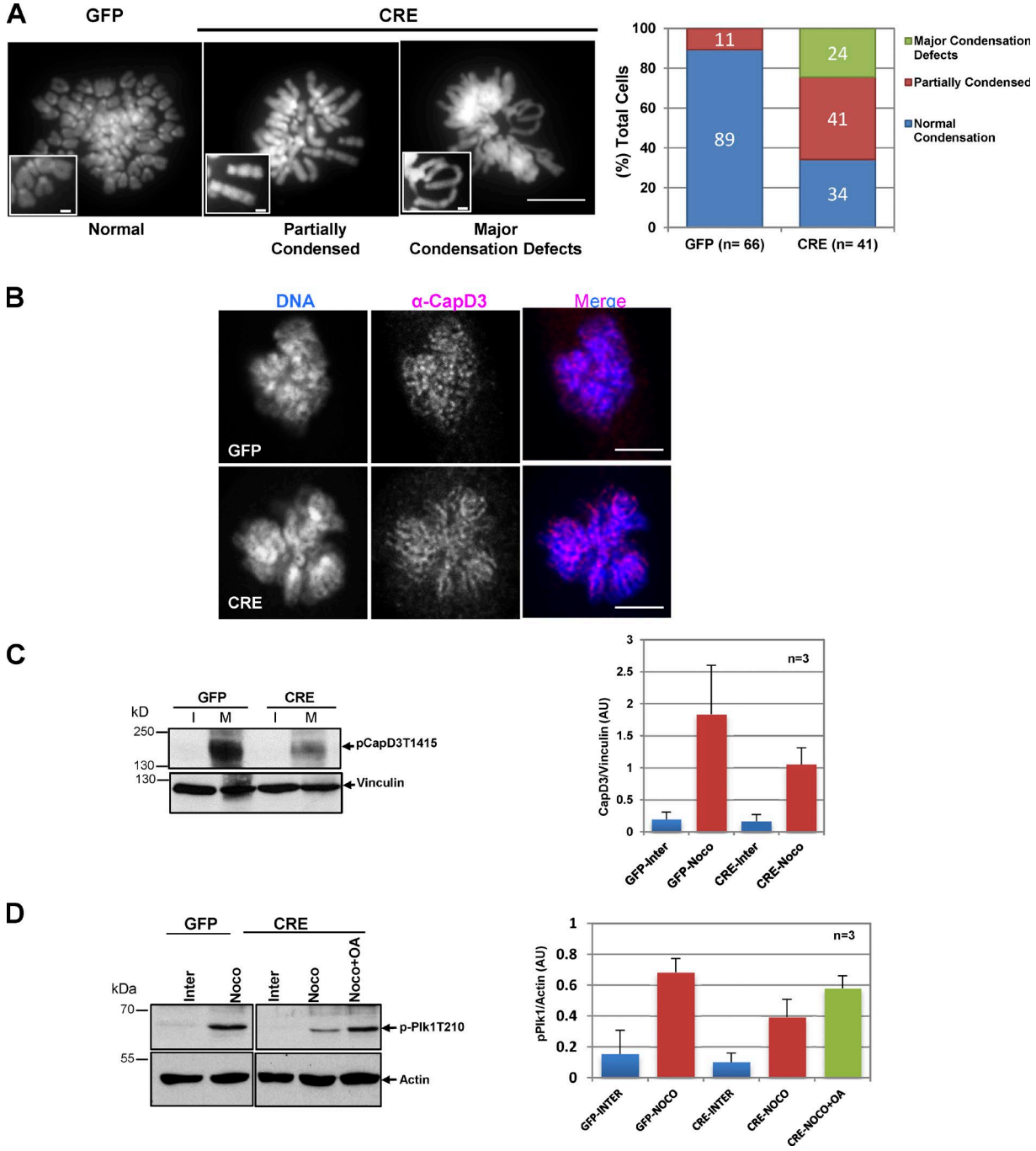


Figure 6. **Partially decondensed DNA in *Arpp19* knockout MEFs is associated with dephosphorylation of histone H3 and of the condensin II subunit CAPD3. (A)** GFP and CRE cells were synchronized in mitosis with nocodazole, and after shake-off, chromosome spreads were prepared. Left: Representative phenotypes observed in chromosome spreads. Right: Quantification of cells displaying the indicated phenotypes. Data were from two independent experiments. **(B)** GFP- or GFP-Cre–transduced MEFs were used for immunofluorescence analysis with anti-CAPD3 antibodies and confocal microscopy (representative images). Bars, 5 µm. Bar magnifications, 2 µm. **(C and D)** Mitotically enriched GFP- or GFP-Cre–transduced *Arpp19*$^{Lox/Lox}$ MEFs were incubated or not with OA, and then lysates were analyzed by Western blotting. Band intensities from three independent experiments were normalized to the loading controls and are represented as the mean ± SD of three replicates.

control in mammals was never investigated. Here, we provide evidence that the mammalian ARPP19 and ENSA paralogs could have different roles, notably during embryogenesis.

We found that *Arpp19* is required throughout mouse embryonic development. *Arpp19* ablation in early embryos or in MEFs dramatically affects mitotic division by perturbing the pattern of dephosphorylation of key proteins involved in mitotic exit. This dephosphorylation would be the consequence of an abnormal reactivation of PP2A in the absence of its inhibitor. Intriguingly, ARPP19 cellular concentration is very low and insufficient to fully inhibit PP2A-B55, raising the possibility that only a partial pool of this phosphatase would be involved in mitotic substrate dephos-

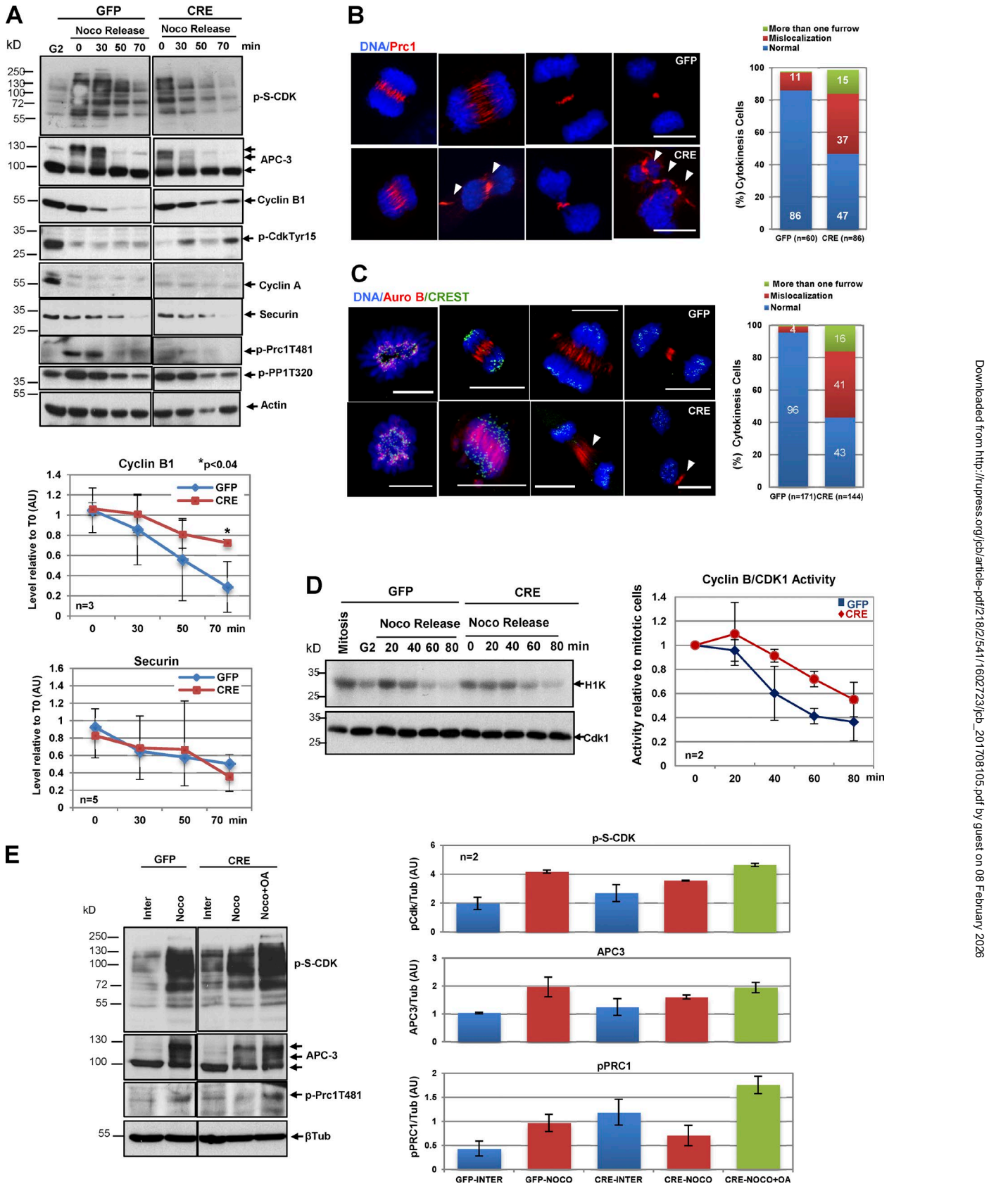


Figure 7. ***Arpp19* ablation promotes premature dephosphorylation of key cyclin B/CDK1 substrates and disrupts the temporal order of events of mitotic exit. (A)** GFP- or GFP-Cre–treated MEFs were enriched in mitosis by nocodazole and isolated by shake-off. Cells were then released and collected at the indicated time points. Cell lysates were analyzed by Western blotting. Cyclin B1 and securin levels were quantified using ImageJ and are represented relative to the G2 levels. **(B and C)** *Arpp19*$^{Lox/Lox}$ transduced MEFs were fixed and incubated with the indicated antibodies, and images were acquired by confocal

phorylation. Unlike ARPP19, ENSA would be dispensable to support correct cell division of the early mouse embryo. Accordingly, *Ensa*-knockout mouse embryos at stage E8.5 were normal. However, our data do not allow us to exclude the possibility that this protein could participate to a lesser extent in embryonic mitotic division. We tried to address this issue by checking the impact of a double deletion of ARPP19 and ENSA in mouse embryogenesis. For this, we constructed an inducible *Arpp19*$^{Lox/Lox}$/*Ensa*$^{Lox/Lox}$/CRE-ERT2–knockout mouse, and we checked whether a double deletion would promote an earlier embryonic block than the one observed in *Arpp19* knockout during gastrulation. Unfortunately, we could not answer this question because the i.p. injection of either tamoxifen or the buffer solution in pregnant females at very early stages of development prevented embryo implantation.

Because ARPP19 and ENSA similarly inhibit PP2A-B55, we also investigated whether ARPP19, like ENSA, could control S phase progression. Our results demonstrate that *Arpp19* ablation does not affect S phase, supporting the hypothesis that ARPP19 and ENSA differentially control cell division, at least in MEFs.

Finally, we showed that in HeLa cells, endogenous ARPP19 is phosphorylated by GWL and binds to PP2A-B55 during mitosis, as in MEFs. This suggests that ARPP19 might participate in the regulation of the PP2A-B55–dependent protein dephosphorylation pattern during mitotic progression also in somatic adult cells.

In summary, we demonstrated that ARPP19 is expressed in mammalian cells and binds to and inhibits PP2A-B55 during mitosis. We also found that ARPP19, and not ENSA, is essential for mouse embryonic cell division, at least until mid-development, by controlling mitotic division. Conversely, we establish that ENSA, but not ARPP19, does regulate S phase in embryonic cells, and probably also in somatic adult cells, highlighting a putative differential regulation and function of these two paralogs in the control of cell division. These data bring an answer to the outstanding question about ARPP19's role in cell cycle control and raise the new important issue of the identification of the regulatory mechanisms conferring to these two proteins their correct temporal and spatial patterns of activation.

## Materials and methods

### Generation of mouse strains lacking *Ensa* or *Arpp19*

The mouse strain carrying the Ensa$^{tm1a(EUCOMM)Hmgu}$ allele was generated in the Immunophenomique Center (Marseilles, France) by blastocyst injection of the embryonic stem cell (ESC) clone HEPDD0901_1_A07 obtained from the European Mouse Mutant Cell Repository. Chimeric mice were crossed with C57BL/6N mice, and germline transmission was verified and confirmed by breeding. The Ensa$^{tm1a(EUCOMM)Hmgu}$ mouse strain was amplified and kept at the heterozygote state by mating WT and heterozygous mice. The mouse strain carrying the Arpp19$^{tm1a(KOMP)Mbp}$ allele was generated in the Institut Clinique de la Souris (Alsace, France) by blastocyst injection of the ESC clone DEPD0006_7_C07 generated by the trans–National Institutes of Health Knockout Mouse Project (KOMP) and obtained from the KOMP Repository. For both *Arpp19* and *Ensa* alleles, before microinjection, the identity of the targeted ESCs was verified by genotyping, sequencing of the 3′ and 5′ ends, vector copy number equal to 1, presence or loss of Y chromosome, and chromosome count. Chimeric mice were bred with C57BL/6N mice, and germline transmission was verified by quantitative PCR to detect the neotransgene included in the mutant in the F1 heterozygous mice. The presence of the downstream LoxP site was verified by PCR. The C57BL/6N-Gt(ROSA)26Sor$^{tm1(ACTB-cre-EGFP)ICS}$ and C57BL/6N-Gt(ROSA)26Sor$^{tm1(FLP1)Dym/Wtsi}$ transgenic mouse lines that express Cre and Flp recombinases were previously described (Birling et al., 2012). Mice were maintained in specific pathogen-free conditions. The care and use of all mice were in accordance with and was approved by the French National Ethic Committee, no. 36 (2016042116041644 and 1138).

### Early embryo analysis

Embryos of five litters obtained from mating *Arpp19*$^{Wt/\Delta}$ mice were recovered at E8.5 or E10.5 for macroscopic analysis. Genotyping was performed using the extra-embryonic tissues. Four supplementary litters were used for histological analysis. Whole embryos were fixed in Bouin's fixative, and serial sections (7 µm thick) were cut and stained with hematoxylin and eosin. E6.5 embryos from two litters from mating heterozygous *Ensa* knockout first or *Arpp19* males and WT females were stained with β-galactosidase as described below.

### LacZ staining of E6.5 embryos

Whole embryos were fixed in a solution containing 2% formaldehyde, 0.2% glutaraldehyde, 0.02% NP-40, and 0.01% sodium deoxycholate in 1× PBS at 4°C for 30 min. They were washed twice in 1× PBS and stained in a solution containing 1 mg/ml 5-bromo-4-chloro-3-indoyl-β-D-galactopyranoside, 5 mM $K_3Fe(CN)_6$, 5 mM $K_4Fe(CN)_6$, and 2 mM $MgCl_2$ in 1× PBS at 37°C overnight and postfixed in 4% PFA.

### Generation of *Arpp19* conditional inducible knockout mice and late embryonic analysis

*Arpp19*$^{Lox/Lox}$ mice were mated with knock-in (Ki) mice harboring a tamoxifen-inducible Cre recombinase (CreERT2) expressed under the control of the RNA pol II locus (129Sv/C57Bl6/CBA(RNA PolII)-CreER$^{T2}$; Guerra et al., 2003). *Arpp19*$^{Lox/+}$; RNA PII-CreERT2$^{Ki/Ki}$ females were mated with *Arpp19*$^{Lox/Lox}$; RNAPII-CreERT2$^{Ki/Ki}$ males, pregnant females received an i.p. injection of 4 mg hydroxytamoxifen in corn oil at E7.5, and embryos were extracted and photographed with a basic camera and genotyped.

microscopy. Arrowheads highlight mislocalization of PRC1 and Aurora B and cytokinesis furrows. Bar, 10 µm. The phenotypes observed in cells from B and C were counted (data from three different experiments). **(D)** CDK1 activity was tested using histone H1 (H1K) as substrate. Mitosis corresponds to nocodazole-arrested GFP-transduced *Arpp19*$^{Lox/Lox}$ MEFs. H1K signals were quantified and corrected to CDK1 levels and are represented as relative to the H1K signal in mitotic cells. Data from two experiments. **(E)** GFP- or GFP-Cre–expressing adenoviruses were synchronized (Noco) or not (Inter) in mitosis by nocodazole block and incubated or not with OA. Cell lysates were analyzed by Western blotting. Signal intensities were measured by densitometry and normalized and are represented as the mean ± SD of two independent experiments.

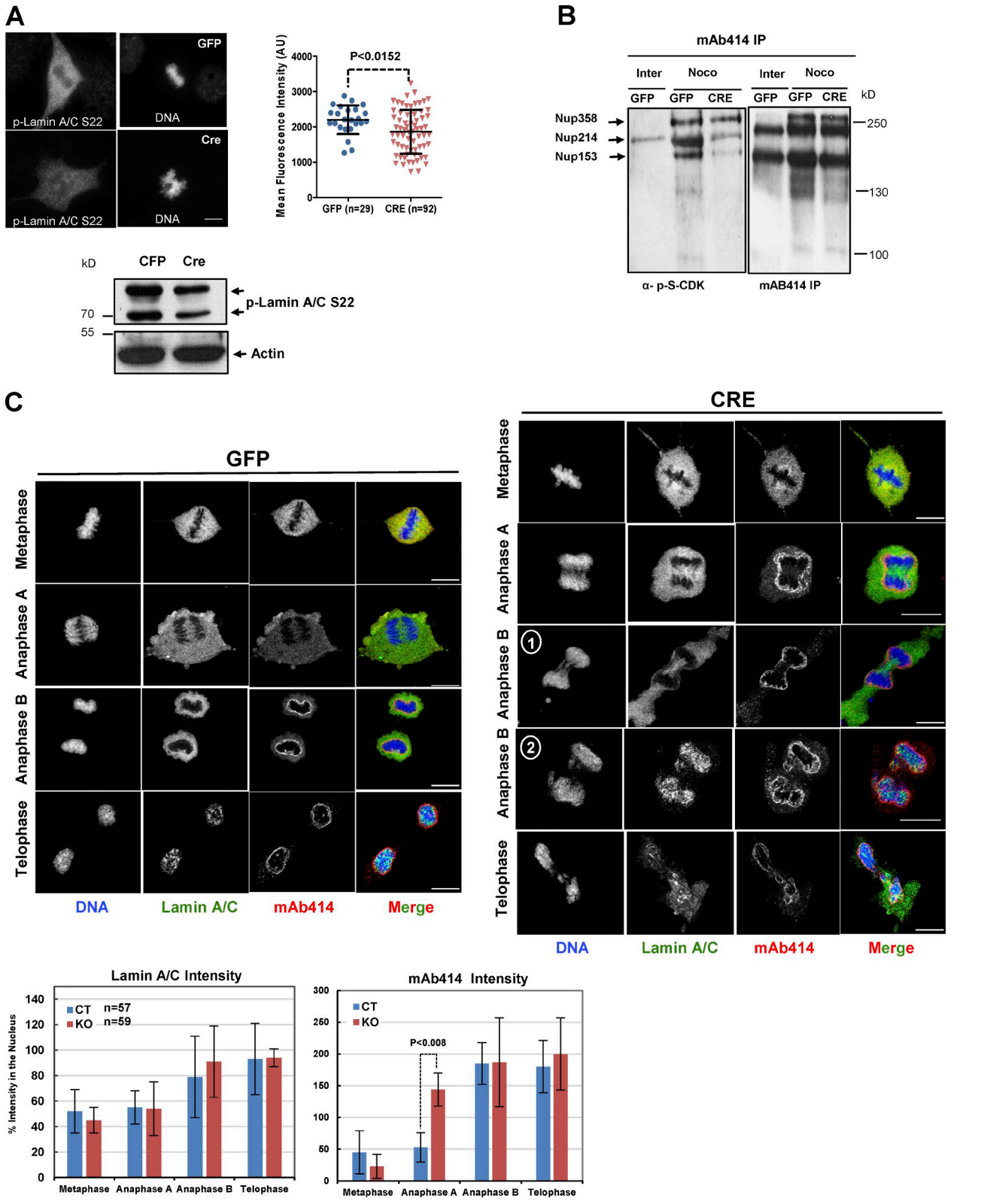


Figure 8. ***Arpp19* knockout perturbs the phosphorylation and localization of key nuclear envelope proteins. (A)** GFP- or GFP-Cre–expressing adenoviruses were enriched in mitotic cells using nocodazole and collected for Western blotting (lower panel) or processed for immunostaining (upper left panel). The phosphorylated lamin A/C at S22 signal was quantified (upper right panel). **(B)** GFP or *Arpp19*$^{\Delta/\Delta}$ MEFs were synchronized (Noco) or not (Inter) in mitosis, lysed, and processed for immunoprecipitation (IP) using the mAB414 antibody that recognizes NUP 358, 214, 153, and 52 (Hofemeister and O'Hare, 2008). IPs were evaluated by Western blotting, using the antibody against serine phosphorylation by CDK (to detect NUP phosphorylation) and mAb414 to measure NUP levels. **(C)** GFP- or GFP-Cre–transduced *Arpp19*$^{Lox/Lox}$ MEFs were analyzed by confocal microscopy using the mAB414 and anti-lamin A/C antibodies. Bar, 10 µm. Lamin A/C and NUP mean intensities during mitosis progression were measured using ImageJ. A line was drawn across the DNA mass

### MEF generation

E13.5 *Arpp19*$^{Lox/Lox}$ embryos were isolated from pregnant females. Head, tail, and organs were discarded, and the remaining tissues were dissected with a scalpel and digested in trypsin-EDTA at 37°C for 1 h, thoroughly dissociated by pipetting, and put in culture in DMEM with 10% FBS. MEFs were immortalized by viral transduction with the large T antigen of SV40 produced in the Platinum-E Retroviral Packing Cell Line based on the pBabe-Large T-SV40 vector.

### Cell culture, transfection, infection, and synchronization

Platinum-E, 293T, and HeLa cells as well as *Arpp19*$^{Lox/Lox}$ primary and immortal MEFs were cultured in DMEM supplemented with 10% FBS. For synchronization experiments, HeLa cells were arrested in G1/S by addition of 2.5 mM thymidine for 24 h. Cells were then washed three times with PBS and released with fresh medium complemented with 25 µM 2′-deoxycytidine. For G2/M synchronization, cells were incubated in 10 µM RO-3306 (Tocris Bioscience) for 12 h. Mitotic cells were obtained by shake-off after 12–14 h of incubation with 100 ng/ml nocodazole.

For *Arpp19* and *Gwl* knockout induction, MEFs were starved in DMEM with 0.1% FBS and then transduced with GFP- or GFP-Cre–expressing adenoviruses (Gene Transfer Core Vector; University of Iowa, Iowa City, IA) for 8 h. After virus washout, MEFs were kept in serum-starvation conditions for 72 h when synchronized in G0 or cultured in DMEM with 10% FBS when used in asynchronous conditions. G1/S synchronization was induced by incubation with 2 µg/ml aphidicolin for 24 h. Mitotic cells were obtained by shake-off after incubation with nocodazole (350 ng/ml for 12–14 h). MEFs were incubated with 5 nM OA for 12 h.

MEFs that stably express the indicate proteins were generated with pMX-puro–, PLPC-puro–, and pMSCV-hygromycin–based retroviral vectors in 293T or Platinum-E cells, respectively, as described previously (Vera et al., 2015). Transduced cells were then selected in hygromycin (40 µg/ml, 7 d) or puromycin (1 µg/ml, 3 d). Empty vector or tag-expressing retroviral vectors were used as controls.

HeLa and U2OS cells were transfected with a scrambled (SC) or two siRNAs against *Ensa* (50 nM/each; siRNA SC, 5′-CTTAGC TACGATCAAGTAC-3′; siRNA Ensa 1 [siE1], 5′-GCCAAGATGAAG AATAAGC-3′ [271–289]; and siRNA Ensa 2 [siE2], 5′-GAAACAAGA AGAAGAGAAC-3′ [9–27]), using Lipofectamine RNAimax (Life Technologies), according to the manufacturer's instructions. siRNAs were synthesized with the T7 RiboMaX Express RNAi system (Promega).

### Cell extract and sample preparation for biochemical analyses

For Western blot and H1 kinase assays, cells were lysed in buffer containing 0.25% Igepal, 150 mM NaCl, 50 mM Tris, and 1 mM EDTA, complemented with 1 mM $Na_3VO_4$, 2 mM NaF, 1 mM PMSF, protease inhibitor cocktail (P8340; Sigma-Aldrich), and 500 nM microcystin-LR (for phosphorylated protein analysis). For treslin Western blot analysis, cells were resuspended in 10 mM Tris, pH 6.8, 1% SDS, 5% glycerol, 100 mM β-mercaptoethanol, and 1 mM DTT and subjected to two pulses of 20-s sonication.

To check CAPD3 phosphorylation on T1415, cells were extracted as described by Abe et al. (2011), in a buffer containing 20 mM Tris-HCl, pH 7.4, 100 mM NaCl, 20 mM β-glycerophosphate, 5 mM $MgCl_2$, 0.1% Triton X-100, 10% glycerol, and 1 mM DTT, supplemented with a cocktail of protease inhibitors, in the presence of 500 nM microcystin-LR, 2 mM $Na_3VO_4$, and 10 mM NaF.

To investigate ARPP19–PP2A interaction, freshly pelleted HeLa cells were lysed in a buffer containing 400 mM Hepes, pH 7.5, 120 mM NaCl, 1% Triton X-100, 1 mM EDTA, and 1 mM DTT and supplemented with 1 mM $Na_3VO_4$, 2 mM NaF, and protease inhibitor cocktail at RT. Reversible cross-linking was then performed by adding dithiobis-succinimidyl propionate at a final concentration of 2.5 mg/ml (Thermo Fisher Scientific) at RT for 30 min and stopped by addition of Tris, pH 7.5, at a final concentration of 200 mM at 4°C for 30 min. Protein extracts were then clarified by centrifugation at 4°C and used for immunoprecipitation.

### Immunoprecipitation experiments

Immunoprecipitation experiments were performed by incubating 400–1,000 µg total protein lysates and 2 µg antibody immobilized on protein A-Dynabeads (Dynal Beads; Invitrogen) at RT for 1 h. Immunoprecipitates were eluted in Laemmli buffer and boiled at 95°C or not (when probing for PP2A-B55 subunits). Elution volumes corresponding to 200–500 µg of total proteins were then analyzed by immunoblotting, as described below.

### Immunoblotting

Total protein extracts (20–50 µg) were separated on polyacrylamide gels and then transferred onto Immobilon-P membranes. Membranes were blocked with 5% milk-TBS-Tween (TBST) and complemented with 5 mM NaF when analyzing phosphorylated proteins. Primary antibodies (Table S1) were diluted in 2% milk-TBST and added at 4°C overnight, and HRP-conjugated secondary antibodies against rabbit (Cell Signaling), mouse, goat, rat (Santa Cruz Biotechnologies), or RecA-HRP (Invitrogen) in 2% milk-TBST were added at RT for 40 min.

### Immunohistochemistry

Cells were grown on coverslips coated with poly-L-lysine (Sigma-Aldrich). To check discrete localizations, a preextraction in PHEM/0.25% Triton X-100 was performed for 30 s before fixation in PHEM/0.25% Triton X-100/3.2% PFA. For staining and total fluorescence signal quantifications, cells were fixed in PHEM/0.25% Triton X-100/3.2% PFA, permeabilized in 0.2%

on the DAPI channel and transposed to the lamin A/C (green) and NUPs (red) channels using the region of interest plug-in. A plot profile was then constructed, and NUP intensity was measured in two points on the profile located outside and at the surface of the DNA mass. The mean values of these two points were then used to calculate the percentage of nuclear NUPs relative to the total intensity. Lamin A/C intensities were calculated as for the NUP signals except that, because of the diffuse nuclear distribution of Lamin A/C, intensities were measured outside and inside the DNA mass. Lamin A/C and NUP intensity data (mean ± SD) are from 57 GFP- and 59 GFP-Cre–transduced MEFs from three different experiments.

Triton X-100 for 4 min, and incubated with primary antibodies in 1.5% BSA/PBS at 37°C for 1 h. Antibodies were revealed with Alexa Fluor 546– or 488–conjugated goat anti-rabbit or mouse antibodies (Life Technologies). Coverslips were mounted with Prolong Gold mounting medium (Invitrogen). Images were taken using an epifluorescence upright (Molecular Devices) wide-field Axioimager Z2 fluorescence microscope (Zeiss) with PL APO ×63 or ×40 objectives (numerical aperture 1.32 and 1.4, respectively; Leica) and a CoolSNAP HQ2 3 camera (Photometrics). When indicated, 1–2-mm confocal immunofluorescence sections were obtained with a Leica SP5-SMD confocal microscope coupled to a photo tunneling microscope driven by LAS AF acquisition software. Objectives 40× HCX Plan Apo CS oil 1.3 NA and 63× HCC Plan Apo CS oil 1.4 NA were used.

Image analysis and intensity measurements were performed using ImageJ software (National Institutes of Health). Maximum projections of confocal images were obtained, and a composite of false-color stacked images was constructed when indicated. When kinetochore intensity was measured, BUBR1 signal was detected with Imaris in 3D images and manually corrected using antikinetochore antibody (CREST) staining. Images in control and perturbed situations were acquired with identical imaging conditions.

### Live imaging

For measuring mitotic kinetics in Fig. 4 A, *Arpp19*$^{Lox/Lox}$ MEFs that stably express PLPC-H2BmCherry were transduced with GFP or GFP-Cre adenoviruses in serum-starved conditions for 72 h and were then forced to reenter the cell cycle by addition of medium with 20% serum. Cells were then maintained in cell culture medium at 37°C and 5% $CO_2$, and Cherry signal was detected with an inverted Olympus IX83 microscope, using a 40× objective, NA 0.6, camera scMOS ZYLA 4.2 MP, driven by Metamorph software (Molecular Devices). The first cell division was monitored. Images were taken every 5 min up to 40 h, using sections of 2 µm and a total of 15 sections.

For high-resolution analyses shown in Fig. 4 C, cells were maintained in culture medium, 37°C, 5% $CO_2$, and H2B-Cherry signal was recorded using time-lapse confocal microscopy with a spinning disk Nikon TI Andor CSU-X1 coupled to an EMCCDiXon897 Andor (512 × 512 pixels) camera. Images were acquired with 22 Z-sections in 1-µm steps, taken every 60–90 s for up to 3 h with a 60×/1.45 NA oil lens. Maximum projections were generated using ImageJ.

### Chromosome spreading

Cells were synchronized in mitosis using 350 ng/ml nocodazole and isolated by shake-off. Cell pellets were resuspended in hypotonic solution (15% FBS and 0.075 M KOH) at 37°C for 10 min. After gently spinning down, cell pellets were fixed by addition of one-fifth volume of fixative solution (3:1 absolute ethanol:acetic acid) and kept at −20°C. A few drops of fixed cells were spread on microscope slides and left to dry at RT. DNA was stained with Hoechst 33342 (Sigma-Aldrich), and slides were mounted by using Prolong Gold mounting medium (Invitrogen).

### In vitro kinase assays

For measuring CDK1 kinase activity, CDK1 was immunoprecipitated from 200 µg total protein extracts prepared at the indicated time points. Immunoprecipitates were then supplemented with 20 µl H1K buffer (50 mM Hepes, pH 7.5, 5 mM $MgCl_2$, 200 µM ATP, and 5 mg/ml histone H1) including 5 µCuries [$\gamma^{33}$]ATP and incubated for 10 min at RT. Reactions were stopped by adding Laemmli sample buffer and analyzed by SDS-PAGE (Lorca et al., 2010).

Casein kinase assays were performed in immunoprecipitates from 200 µg total protein extracts. Immunoprecipitates were incubated in 20 µl of a mix containing 1 mg/ml dephosphorylated α-casein, 100 µM ATP (200 cpm/pm), 2 mM $MgCl_2$, and 50 mM Tris-HCl, pH 7.5. Incubations were terminated by addition of Laemmli buffer, and then proteins were separated by SDS-PAGE and phosphorylation rates estimated by autoradiography.

### Cell viability

*Arpp19*$^{\Delta/\Delta}$ MEFs that stably expressed (or not) WT ARPP19 or the S62A mutant were seeded in 60-mm plates and maintained in culture for 2 to 3 wk until foci were evident. Cells were then fixed and stained with 70% ethanol/1% crystal violet for 5 min and washed, and colonies were counted.

### EdU labeling

Cells were grown on glass coverslips and pulsed with 10 µM EdU for 30 min, washed once with PBS, and fixed in PBS with 3.2% formaldehyde for 15 min. Cells were then permeabilized in 0.2% Triton X-100 for 10 min and blocked (3% BSA and 0.1% Tween-20 in PBS) for 45 min. Click-iT EdU Alexa Fluor 530 staining was performed according to the manufacturer's instructions (Invitrogen). After DNA staining with Hoechst 33342 (Sigma-Aldrich), coverslips were mounted with Prolong Gold mounting medium (Invitrogen), and images were captured as described above. An ImageJ automated macro was used to quantify EdU signal within the nucleus and to count the number of replicating cells.

### FACS

For FACS, cells were fixed in chilled 70% ethanol at −20°C, washed with PBS, and DNA stained with a solution containing propidium iodide (5 µg/ml) and RNase A (0.5 mg/ml) in PBS (Burgess et al., 2010). Cells were analyzed on a FACS Calibur (BD Biosciences) using Cell Quest Pro (BD Biosciences) and Flow Jo software. FACS sorting was performed on FACS Aria II U (BD Biosciences) with FACSDiva software.

### Antibody production and purification

For the Nter-ARPP19 antibody, 120 nucleotides of the human ARPP19 sequence were cloned in the pET15-6His vector (Table S2). The fusion protein was expressed in *Escherichia coli* cells and purified using a nickel column. Purified ARPP19 was then used for rabbit immunization, and the collected serum was affinity purified on immobilized ARPP19 MBP-fusion protein (Table S1).

For the PanB55 antibody, GST-tagged *X. laevis* B55 delta was produced, purified, and used for rabbit immunization. Serum was exhausted of the His tag and affinity purified on immobilized GST–*X. laevis* B55 delta fusion protein.

### Statistics

Average (mean), SD, or SEM and statistical significance based on two-tailed Student's test were calculated using Microsoft Excel. P values are indicated in the figures.

### Ethics statement

All procedures were conducted in accordance with the Guide for the Care and Use of Laboratory Animals (Institute of Laboratory Animal Resources, 2011) and were approved by the French Ethic Committee no. 36, Languedoc-Roussillon (2016042116041644, 201607041221601, and 1138).

### Online supplemental material

Fig. S1 shows that embryonic cells display similar ARPP19 and ENSA transcription. Fig. S2 shows that *Arpp19*, but not *Ensa*, ablation in primary MEFs results in dramatic mitotic phenotypes. Video 1 shows the first mitotic division of GFP-transduced *Arpp19*$^{Lox/Lox}$ MEFs and Videos 2, 3, 4, and 5 the GFP-CRE–transduced *Arpp19*$^{Lox/Lox}$ MEFs. Table S1 lists antibodies used in the study, and Table S2 lists plasmids used.

## Acknowledgments

We thank V. Georget, S. De Rossi, and M. Boyer from Montpellier Ressources Imagerie (Montpellier, France); F. Lionneton and S. Fromont for the Montpellier Genomic Collection facility; P. Richard and M. Plays for the antibody facility (Centre de Recherche de Biologie Cellulaire de Montpellier [CRBM], Montpellier, France); S. Coudrec for the Mouse Animal facility (Institut de Génétique Moléculaire de Montpellier Montpellier, France); M. Jagla-Eberlin, T. Sorg, and O. Wendling from Phenomin-Institute Clinic de la Souris (Illkirch, France); F. Fiore from Centre d'Immunophénomique (Marseille, France) for mouse model establishment; and the Viral Vector Core Facility (University of Iowa, Iowa City, IA) for vector production. We are indebted to L. Munoz and S. Ovejero (Centro de Investigacion del Cancer, Salamanca, Spain) for help in MEF purification, to T. Hirota (Cancer Institute, Tokyo, Japan), and A. Losada (Centro Nacional de Investigaciones Oncológicas [CNIO], Madrid, Spain) for the anti-phospho-CAPD3 and anti-CAPD3 antibodies, respectively; to L. Le Cam, M. Lacroix, and G. Rodier (L'Institut de Recherche en Cancérologie de Montpellier, Montpellier, France); and to N. Morin (CRBM) for valuable advice and reagents. We are indebted to M. Malumbres (CNIO) for GWL$^{Lox/Lox}$ MEFs, and, finally, we thank L. Longin for help in key experiments and the other Castro-Lorca laboratory members for fruitful discussions.

This work was supported by the Labex EpiGenMed, Agence Nationale de la Recherche "Investissement d'avenir" program (ANR-10-LABX-12-01), the Fondation pour la Recherche Médicale "Equipes FRM 2015," and Ligue Contre le Cancer "Equipe Labelisée." K. Hached was supported by the Fondation ARC pour la Recherche sur le Cancer and the Labex EpiGenMed, and P. Goguet by the Labex EpiGenMed and the Fondation de France. National Institutes of Health, National Human Genome Research Institute grants U01HG004085 to Velocigene at Regeneron Inc. (Tarrytown, NY) and U01HG004080 to the Consortium of CHO RI, the Sanger Institute, and University of California, Davis (CSD), that funded the generation of gene-targeted ESCs for 8,500 genes in the Knockout Mouse Project.

The authors declare no competing financial interests.

Author contributions: K. Hached and P. Goguet designed and performed most of the experiments and analyzed the data. S. Charrasse contributed to immunofluorescence staining and analysis and treslin Western blot analysis. S. Vigneron helped with the biochemical and molecular biology techniques. M.P. Sacristan helped with MEF purification. T. Lorca designed the experiments with those performing them, analyzed the data, and participated in discussions. A. Castro designed the experiments with those performing them, analyzed the data, and wrote the manuscript.

Submitted: 16 August 2017
Revised: 5 October 2018
Accepted: 21 November 2018

## References

Abe, S., K. Nagasaka, Y. Hirayama, H. Kozuka-Hata, M. Oyama, Y. Aoyagi, C. Obuse, and T. Hirota. 2011. The initial phase of chromosome condensation requires Cdk1-mediated phosphorylation of the CAP-D3 subunit of condensin II. *Genes Dev.* 25:863–874. https://doi.org/10.1101/gad.2016411

Birling, M.C., A. Dierich, S. Jacquot, Y. Hérault, and G. Pavlovic. 2012. Highly-efficient, fluorescent, locus directed cre and FlpO deleter mice on a pure C57BL/6N genetic background. *Genesis.* 50:482–489. https://doi.org/10.1002/dvg.20826

Burgess, A., S. Vigneron, E. Brioudes, J.-C. Labbé, T. Lorca, and A. Castro. 2010. Loss of human Greatwall results in G2 arrest and multiple mitotic defects due to deregulation of the cyclin B-Cdc2/PP2A balance. *Proc. Natl. Acad. Sci. USA.* 107:12564–12569. https://doi.org/10.1073/pnas.0914191107

Castilho, P.V., B.C. Williams, S. Mochida, Y. Zhao, and M.L. Goldberg. 2009. The M phase kinase Greatwall (Gwl) promotes inactivation of PP2A/B55delta, a phosphatase directed against CDK phosphosites. *Mol. Biol. Cell.* 20:4777–4789. https://doi.org/10.1091/mbc.e09-07-0643

Charrasse, S., A. Gharbi-Ayachi, A. Burgess, J. Vera, K. Hached, P. Raynaud, E. Schwob, T. Lorca, and A. Castro. 2017. Ensa controls S-phase length by modulating Treslin levels. *Nat. Commun.* 8:206–220. https://doi.org/10.1038/s41467-017-00339-4

Chica, N., A.E. Rozalén, L. Pérez-Hidalgo, A. Rubio, B. Novak, and S. Moreno. 2016. Nutritional Control of Cell Size by the Greatwall-Endosulfine-PP2A·B55 Pathway. *Curr. Biol.* 26:319–330. https://doi.org/10.1016/j.cub.2015.12.035

Cundell, M.J., R.N. Bastos, T. Zhang, J. Holder, U. Gruneberg, B. Novak, and F.A. Barr. 2013. The BEG (PP2A-B55/ENSA/Greatwall) pathway ensures cytokinesis follows chromosome separation. *Mol. Cell.* 52:393–405. https://doi.org/10.1016/j.molcel.2013.09.005

Ferrell, J.E. Jr. 2013. Feedback loops and reciprocal regulation: recurring motifs in the systems biology of the cell cycle. *Curr. Opin. Cell Biol.* 25:676–686. https://doi.org/10.1016/j.ceb.2013.07.007

Gharbi-Ayachi, A., J.C. Labbé, A. Burgess, S. Vigneron, J.M. Strub, E. Brioudes, A. Van-Dorsselaer, A. Castro, and T. Lorca. 2010. The substrate of Greatwall kinase, Arpp19, controls mitosis by inhibiting protein phosphatase 2A. *Science.* 330:1673–1677. https://doi.org/10.1126/science.1197048

Glover, D.M. 2012. The overlooked greatwall: a new perspective on mitotic control. *Open Biol.* 2:120023. https://doi.org/10.1098/rsob.120023

Guerra, C., N. Mijimolle, A. Dhawahir, P. Dubus, M. Barradas, M. Serrano, V. Campuzano, and M. Barbacid. 2003. Tumor induction by an endogenous K-ras oncogene is highly dependent on cellular context. *Cancer Cell.* 4:111–120. https://doi.org/10.1016/S1535-6108(03)00191-0

Heald, R., and F. McKeon. 1990. Mutations of phosphorylation sites in lamin A that prevent nuclear lamina disassembly in mitosis. *Cell.* 61:579–589. https://doi.org/10.1016/0092-8674(90)90470-Y

Hofemeister, H., and P. O'Hare. 2008. Nuclear pore composition and gating in herpes simplex virus-infected cells. *J. Virol.* 82:8392–8399. https://doi.org/10.1128/JVI.00951-08

Hunt, T. 2013. On the regulation of protein phosphatase 2A and its role in controlling entry into and exit from mitosis. *Adv. Biol. Regul.* 53:173–178. https://doi.org/10.1016/j.jbior.2013.04.001

Jiang, W., G. Jimenez, N.J. Wells, T.J. Hope, G.M. Wahl, T. Hunter, and R. Fukunaga. 1998. PRC1: a human mitotic spindle-associated CDK substrate protein required for cytokinesis. *Mol. Cell.* 2:877–885. https://doi.org/10.1016/S1097-2765(00)80302-0

Juanes, M.A., R. Khoueiry, T. Kupka, A. Castro, I. Mudrak, E. Ogris, T. Lorca, and S. Piatti. 2013. Budding yeast greatwall and endosulfines control activity and spatial regulation of PP2A(Cdc55) for timely mitotic progression. *PLoS Genet.* 9:e1003575. https://doi.org/10.1371/journal.pgen.1003575

Kim, M.Y., E. Bucciarelli, D.G. Morton, B.C. Williams, K. Blake-Hodek, C. Pellacani, J.R. Von Stetina, X. Hu, M.P. Somma, D. Drummond-Barbosa, and M.L. Goldberg. 2012. Bypassing the Greatwall-Endosulfine pathway: plasticity of a pivotal cell-cycle regulatory module in Drosophila melanogaster and Caenorhabditis elegans. *Genetics.* 191:1181–1197. https://doi.org/10.1534/genetics.112.140574

Kschonsak, M., and C.H. Haering. 2015. Shaping mitotic chromosomes: From classical concepts to molecular mechanisms. *BioEssays.* 37:755–766. https://doi.org/10.1002/bies.201500020

Li, Y.H., H. Kang, Y.N. Xu, Y.T. Heo, X.S. Cui, N.H. Kim, and J.S. Oh. 2013. Greatwall kinase is required for meiotic maturation in porcine oocytes. *Biol. Reprod.* 89:53. https://doi.org/10.1095/biolreprod.113.109850

Lorca, T., and A. Castro. 2013. The Greatwall kinase: a new pathway in the control of the cell cycle. *Oncogene.* 32:537–543. https://doi.org/10.1038/onc.2012.79

Lorca, T., C. Bernis, S. Vigneron, A. Burgess, E. Brioudes, J.C. Labbé, and A. Castro. 2010. Constant regulation of both the MPF amplification loop and the Greatwall-PP2A pathway is required for metaphase II arrest and correct entry into the first embryonic cell cycle. *J. Cell Sci.* 123:2281–2291. https://doi.org/10.1242/jcs.064527

Martín, R., M. Portantier, N. Chica, M. Nyquist-Andersen, J. Mata, and S. Lopez-Aviles. 2017. A PP2A-B55-Mediated Crosstalk between TORC1 and TORC2 Regulates the Differentiation Response in Fission Yeast. *Curr. Biol.* 27:175–188. https://doi.org/10.1016/j.cub.2016.11.037

Mellone, B.G., L. Ball, N. Suka, M.R. Grunstein, J.F. Partridge, and R.C. Allshire. 2003. Centromere silencing and function in fission yeast is governed by the amino terminus of histone H3. *Curr. Biol.* 13:1748–1757. https://doi.org/10.1016/j.cub.2003.09.031

Mochida, S. 2014. Regulation of α-endosulfine, an inhibitor of protein phosphatase 2A, by multisite phosphorylation. *FEBS J.* 281:1159–1169. https://doi.org/10.1111/febs.12685

Mochida, S., S. Ikeo, J. Gannon, and T. Hunt. 2009. Regulated activity of PP2A-B55 delta is crucial for controlling entry into and exit from mitosis in Xenopus egg extracts. *EMBO J.* 28:2777–2785. https://doi.org/10.1038/emboj.2009.238

Mochida, S., S.L. Maslen, M. Skehel, and T. Hunt. 2010. Greatwall phosphorylates an inhibitor of protein phosphatase 2A that is essential for mitosis. *Science.* 330:1670–1673. https://doi.org/10.1126/science.1195689

Mochida, S., S. Rata, H. Hino, T. Nagai, and B. Novák. 2016. Two Bistable Switches Govern M Phase Entry. *Curr. Biol.* 26:3361–3367. https://doi.org/10.1016/j.cub.2016.10.022

Peters, J.M. 2006. The anaphase promoting complex/cyclosome: a machine designed to destroy. *Nat. Rev. Mol. Cell Biol.* 7:644–656. https://doi.org/10.1038/nrm1988

Skarnes, W.C., B. Rosen, A.P. West, M. Koutsourakis, W. Bushell, V. Iyer, A.O. Mujica, M. Thomas, J. Harrow, T. Cox, et al. 2011. A conditional knockout resource for the genome-wide study of mouse gene function. *Nature.* 474:337–342. https://doi.org/10.1038/nature10163

St-Pierre, J., M. Douziech, F. Bazile, M. Pascariu, E. Bonneil, V. Sauvé, H. Ratsima, and D. D'Amours. 2009. Polo kinase regulates mitotic chromosome condensation by hyperactivation of condensin DNA supercoiling activity. *Mol. Cell.* 34:416–426. https://doi.org/10.1016/j.molcel.2009.04.013

Talarek, N., E. Cameroni, M. Jaquenoud, X. Luo, S. Bontron, S. Lippman, G. Devgan, M. Snyder, J.R. Broach, and C. De Virgilio. 2010. Initiation of the TORC1-regulated G0 program requires Igo1/2, which license specific mRNAs to evade degradation via the 5′-3′ mRNA decay pathway. *Mol. Cell.* 38:345–355. https://doi.org/10.1016/j.molcel.2010.02.039

Talarek, N., E. Gueydon, and E. Schwob. 2017. Homeostatic control of START through negative feedback between Cln3-Cdk1 and Rim15/Greatwall kinase in budding yeast. *eLife.* 6:e26233. https://doi.org/10.7554/eLife.26233

Vera, J., L. Lartigue, S. Vigneron, G. Gadea, V. Gire, M. Del Rio, I. Soubeyran, F. Chibon, T. Lorca, and A. Castro. 2015. Greatwall promotes cell transformation by hyperactivating AKT in human malignancies. *eLife.* 4:e10115. https://doi.org/10.7554/eLife.10115

Vigneron, S., E. Brioudes, A. Burgess, J.C. Labbé, T. Lorca, and A. Castro. 2009. Greatwall maintains mitosis through regulation of PP2A. *EMBO J.* 28:2786–2793. https://doi.org/10.1038/emboj.2009.228

Vigneron, S., L. Sundermann, J.C. Labbé, L. Pintard, O. Radulescu, A. Castro, and T. Lorca. 2018. Cyclin A-cdk1-dependent phosphorylation of Bora is the triggering factor promoting mitotic entry. *Dev. Cell.* 45:637–650.e7. https://doi.org/10.1016/j.devcel.2018.05.005

Wei, Y., L. Yu, J. Bowen, M.A. Gorovsky, and C.D. Allis. 1999. Phosphorylation of histone H3 is required for proper chromosome condensation and segregation. *Cell.* 97:99–109. https://doi.org/10.1016/S0092-8674(00)80718-7

Williams, B.C., J.J. Filter, K.A. Blake-Hodek, B.E. Wadzinski, N.J. Fuda, D. Shalloway, and M.L. Goldberg. 2014. Greatwall-phosphorylated Endosulfine is both an inhibitor and a substrate of PP2A-B55 heterotrimers. *eLife.* 3:e01695. https://doi.org/10.7554/eLife.01695

Wu, J.Q., J.Y. Guo, W. Tang, C.S. Yang, C.D. Freel, C. Chen, A.C. Nairn, and S. Kornbluth. 2009. PP1-mediated dephosphorylation of phosphoproteins at mitotic exit is controlled by inhibitor-1 and PP1 phosphorylation. *Nat. Cell Biol.* 11:644–651. https://doi.org/10.1038/ncb1871

Xing, Y., Y. Xu, Y. Chen, P.D. Jeffrey, Y. Chao, Z. Lin, Z. Li, S. Strack, J.B. Stock, and Y. Shi. 2006. Structure of protein phosphatase 2A core enzyme bound to tumor-inducing toxins. *Cell.* 127:341–353. https://doi.org/10.1016/j.cell.2006.09.025

Yeong, F.M., H. Hombauer, K.S. Wendt, T. Hirota, I. Mudrak, K. Mechtler, T. Loregger, A. Marchler-Bauer, K. Tanaka, J.M. Peters, and E. Ogris. 2003. Identification of a subunit of a novel Kleisin-beta/SMC complex as a potential substrate of protein phosphatase 2A. *Curr. Biol.* 13:2058–2064. https://doi.org/10.1016/j.cub.2003.10.032